Upwind methods for the Baer-Nunziato equations and higher-order reconstruction using artificial viscosity

F. Fraysse[a,b], C. Redondo[b], G. Rubio[b], E. Valero[b]

[a] *RS2N. St. Zacharie. France.*
[b] *E. T. S. de Ingeniería Aeronáutica y del Espacio (Universidad Politécnica de Madrid). Madrid. Spain.*

Abstract

This article is devoted to the numerical discretisation of the hyperbolic two-phase flow model of Baer and Nunziato. A special attention is paid on the discretisation of intercell flux functions in the framework of Finite Volume and Discontinuous Galerkin approaches, where care has to be taken to efficiently approximate the non-conservative products inherent to the model equations. Various upwind approximate Riemann solvers have been tested on a bench of discontinuous test cases. New discretisation schemes are proposed in a Discontinuous Galerkin framework following the criterion of Abgrall and the path-conservative formalism. A stabilisation technique based on artificial viscosity is applied to the high-order Discontinuous Galerkin method and compared against classical TVD-MUSCL Finite Volume flux reconstruction.

Keywords: Two-phase, upwind, high-order, Discontinuous Galerkin

1. Introduction

Nowadays, numerical computation of multiphase fluid dynamics problems involving complex physical phenomena is becoming affordable. Many industrial sectors have to deal with fluid flows composed of various phases in interaction such as the nuclear industry (reactor safety, cooling, detonation), the aerospace (solid or liquid propulsion, ice formation, reentry vehicles), the oil and gas (extraction, transport, fracturing) and many others now and in the future. While experiments are very handful to validate theoretical models, in many cases the set up is not possible or too expensive. Direct numerical simulation of multiphase flow problems remain too expensive for industrial applications and today only a few academical attempts are realizable. Thus, many average models have been developed and studied both theoretically and numerically. Among the averaged two-phase flow model equations the set of Baer and Nunziato [1] is becoming more and more attractive since it is hyperbolic unless in some well established circumstances. It is composed of seven equations in one-dimension, continuity, momentum and energy balance for each phase and a convection equation for the volume fraction. The model does not make any assumption on mechanical, thermal or chemical equilibrium, thus, two pressure, velocity and temperatures are present. The main challenge of this set of equations is that it cannot be cast in conservative (or divergence) form because of the presence of non-conservative products. As a consequence, classical Rankine-Hugoniot conditions cannot be used to define the jumps across the contact discontinuities

Email address: francois.fraysse@rs2n.eu (F. Fraysse)

and shocks. This issue has remained challenging for a long time but recently some authors published different methods in order to treat these additional terms [2, 3, 4, 5]. One of the objectives of this article is to review these methods and compare them against each other.

Most works in the literature use a Finite Volume methodology to discretise the Baer and Nunziato model equations. While this approach has interesting features, it is often limited to second-order of accuracy. Attempts to reconstruct Finite Volume methodology to higher order seems promising but suffer from a lack of compactness, which is a bottleneck for massive parallel implementation. On the other hand, Discontinuous Galerkin methods take the advantages of Finite Volume approach (conservation, interface jumps, compactness) but naturally allows the solution to be represented by a high-order polynomial. The second objective of this work is to develop a Discontinuous Galerkin formulation able to solve the Baer-Nunziato equations with a high-order (typically $>$ 2) in the presence of strong discontinuities. The Discontinuous Galerkin spectral element method (DGSEM) [6, 7, 8, 9, 10] will be taken as a basis for the developed method. A special treatment to avoid oscillations in the vicinity of shocks and contact discontinuities is presented. The method is based on artificial viscosity of Persson *et al.* [11].

The paper is organized as follows: in Sec. 2 the discretisation of the Baer-Nunziato equations is presented. The Discontinuous Galerkin method is detailed as well as the upwind fluxes and the treatment of the non-conservative products. High-order flux functions formulations are developed following the criterion of Abgrall and also a path-conservative formalism. In Sec. 3, a bench of one-dimensional test cases is used to assess the accuracy of each upwind flux when a low-order discretisation is employed (Finite Volume). Finally, in Sec. 4, the numerical scheme is tested using high order solution representation and compared against classical TVD-MUSCL Finite Volume flux reconstruction.

2. Discretisation of the two-phase two-pressure model of Baer and Nunziato

The one-dimensional set of Baer-Nunziato equations reads:

$$\frac{\partial \mathbf{U}}{\partial t} + \frac{\partial \mathbf{F}(\mathbf{U})}{\partial x} + \mathbf{H}(\mathbf{U})\frac{\partial \alpha_l}{\partial x} = 0$$

where

$$\mathbf{U} = \begin{bmatrix} \alpha_l \\ \alpha_l\rho_l \\ \alpha_l\rho_l u_l \\ \alpha_l\rho_l E_l \\ \alpha_g\rho_g \\ \alpha_g\rho_g u_g \\ \alpha_g\rho_g E_g \end{bmatrix} \quad \mathbf{F}(\mathbf{U}) = \begin{bmatrix} 0 \\ \alpha_l\rho_l u_l \\ \alpha_l\rho_l u_l^2 + p_l \\ \alpha_l\rho_l u_l H_l \\ \alpha_g\rho_g u_g \\ \alpha_g\rho_g u_g^2 + p_g \\ \alpha_g\rho_g u_g H_g \end{bmatrix} \quad \mathbf{H}(\mathbf{U}) = \begin{bmatrix} u_{int} \\ 0 \\ -p_{int} \\ -p_{int}u_{int} \\ 0 \\ p_{int} \\ p_{int}u_{int} \end{bmatrix}$$

This system of equations is closed with an equation of state for each phase $m = g, l$ (gas and liquid) relating the internal energy $e_m = E_m - 0.5u_m^2$ to the density ρ_m and pressure p_m, the saturation condition $\alpha_l + \alpha_g = 1$

(liquid and gas volume fractions) and finally appropriate interfacial pressure and velocity. In this work, stiffened gas equation is considered for the liquid phase, $e_m = \rho_m e_m(\gamma_m - 1) + \pi_m$, and perfect gas law for the gas phase ($\pi_g = 0$). The interfacial quantities are set according to the choice of Baer and Nunziato: $u_{int} = u_l, p_{int} = p_g$. Details of the eigenstructure of the model can be found in AppendixA.

2.1. ***Discontinuous Galerkin Spectral Element Method***

Discontinuous Galerkin methods were first introduced by Reed and Hill [12] to solve the neutron transport equation. They have emerged in recent years as an efficient and flexible method to solve convection dominated problems [13, 14]. The Discontinuous Galerkin Spectral Element Method (DGSEM) [6, 7, 8, 9, 10, 15] can be seen as a Spectral Element Method (SEM) [16] where the continuity requirement across element boundaries is relaxed, or as a high order Finite Volume (FV) [17] method with a compact stencil. As in a usual FV method, the Riemann Solver [18] stabilises the solution. However in this case higher accuracy may be achieved by increasing the order of the approximation, N, as well as by reducing the size of the elements, h. The DGSEM is used in a wide range of applications such as compressible flows [19, 20], electromagnetics and optics [21, 22, 23, 24], heat transfer [25], aeroacoustics [26, 27, 28, 29], meteorology [30, 31, 32], and geophysics [33, 34].

Discontinuous Galerkin methods were originally developed to solve conservation laws,

$$\frac{\partial \mathbf{U}}{\partial t} + \nabla \cdot \mathbf{F} = 0 \tag{1}$$

A particular nodal variant of the discontinuous Galerkin technique is used here, the Discontinuous Galerkin Spectral Element Method (DGSEM), see Kopriva [10], which solves Eq. 1 in general three-dimensional geometries in which the domain Ω is divided into k non-overlapping quadrilateral elements Ω^k. In this paper, the approximation is restricted, without loss of generality, to two-dimensional problems. Each element in the domain is mapped individually onto a unit square by an iso-parametric transformation. This mapping between the unit square and the physical space is described generically by $\mathbf{x} = \mathbf{r}(\xi, \eta)$ where ξ, η are the computational coordinates on the unit square. For a complete derivation of the DGSEM method, the reader is referred to Kopriva [10]. On each element the solution is approximated by a series of orthogonal (w.r.t. the L_2 inner product) polynomials P_N of degree N, for more information see Canuto *et al.* [16]. As a basis for this approximation, a set of Lagrange interpolating polynomials $\ell_j(\xi), j = 0, ..., N$ is used and can be written as

$$\ell_j(\xi) = \prod_{\substack{i=0 \\ i \neq j}}^{N} \frac{\xi - \xi_i}{\xi_j - \xi_i}. \tag{2}$$

The nodal points, ξ_i, which will become the grid points of the scheme, are chosen to be the nodes of the Legendre-Gauss quadrature. Multiple space dimensions are spanned by tensor products of these polynomials, so that we write $P_{N,N} = P_N \times P_N$. For simplicity of exposition only, we will take the same polynomial order in each direction, though this is not required in practice. From this point onwards and to simplify the notation, we consider that no mapping is performed, i.e. only the reference element in the computational space is used. In two dimensions, the spectral element method approximates the solution and the fluxes element-by-element

by the polynomials

$$\mathbf{U}^N(\xi,\eta) = \sum_{\mu,\nu=0}^{N} \mathbf{U}^N_{\mu,\nu}\phi_{\mu,\nu}, \quad \mathbf{F}^N(\xi,\eta) = \sum_{\mu,\nu=0}^{N} \mathbf{F}^N_{\mu,\nu}\phi_{\mu,\nu} \tag{3}$$

where $\phi_{\mu,\nu} = \ell_\mu(\xi)\,\ell_\nu(\eta)$. The nodal (grid point) values of the fluxes are computed from the grid point values of the solution, i.e. $\mathbf{F}^N_{\mu,\nu} = \mathbf{F}\left(u^N_{\mu,\nu}\right)$. Note that $\mathbf{U}^N_{\mu,\nu}$ is not the nodal value of $\mathbf{U}(\xi,\eta)$, but the result of solving the discretised PDE. Therefore we distinguish

$$\mathbf{U}^N(\xi,\eta) = \sum_{\mu,\nu=0}^{N} \mathbf{U}^N_{\mu,\nu}\phi_{\mu,\nu}, \quad \text{and} \quad I_N\mathbf{U}(\xi,\eta) = \sum_{\mu,\nu=0}^{N} \mathbf{U}_{\mu,\nu}\phi_{\mu,\nu} \tag{4}$$

The former is the solution of the discretised PDE while the latter is the spectral interpolation of the exact solution of the PDE. The same applies to the fluxes

$$\mathbf{F}^N(\xi,\eta) = \sum_{\mu,\nu=0}^{N} \mathbf{F}^N_{\mu,\nu}\phi_{\mu,\nu}, \quad \text{and} \quad I_N\mathbf{F}(\xi,\eta) = \sum_{\mu,\nu=0}^{N} \mathbf{F}_{\mu,\nu}\phi_{\mu,\nu} \tag{5}$$

As generally imposed in variational formulations, the PDE residual is required to be orthogonal to the approximation space locally within an element. Thus,

$$\left(\mathbf{U}^N_t, \phi_{i,j}\right) + \left(\nabla\cdot\mathbf{F}^N, \phi_{i,j}\right) = 0 \quad i,j = 0,1,\ldots,N \tag{6}$$

where $(u,v) = \int_{-1}^{1} uv dx$ represents the usual L^2 inner product. Integration of (6) by parts gives

$$\left(\mathbf{U}^N_t, \phi_{i,j}\right) + \sum_{e\in\partial\Omega}\int_e \mathbf{F}^N\cdot\mathbf{n}\phi_{i,j}dS - \left(\mathbf{F}^N, \nabla\phi_{i,j}\right) = 0 \quad i,j = 0,1,\ldots,N \tag{7}$$

where $\partial\Omega$ represents the boundary of the element and the summation is extended over the edges e of $\partial\Omega$.

To solve these equations, the integrals are replaced by Legendre-Gauss quadratures, which in two dimensional rectangular domains have the property

$$\int_{-1}^{1}\int_{-1}^{1} v(\xi,\eta)\,d\xi d\eta = \sum_{i,j=0}^{N} v(\xi_i,\eta_j)\,w_i w_j \quad \forall v \in P_{2N+1,2N+1} \tag{8}$$

This replacement is exact provided that the element sides are straight. If the sides are curved a quadrature error is incurred in the evaluation of $\left(\mathbf{U}^N_t, \phi_{i,j}\right)$ and in the evaluation of the fluxes. Finally, substituting (3) into (7), taking into account (8) and the discrete orthogonality of the Lagrange interpolating polynomials yields [16]

$$\mathbf{U}^N_{t_{i,j}} w_i w_j + \sum_{e\in\partial\Omega}\int_e \mathbf{F}^N\cdot\mathbf{n}\phi_{i,j}dS - \sum_{\mu,\nu=0}^{N} \mathbf{F}^N_{\mu,\nu}\cdot\nabla\phi_{i,j}w_\mu w_\nu = 0 \quad i,j = 0,1,\ldots,N \tag{9}$$

In (9), $\sum_{e\in\partial\Omega}\int_e \mathbf{F}^N\cdot\mathbf{n}\phi_{i,j}dS$ is the sum of all the integrals over all the edges of the element approximated by quadrature. The boundary term can be written as follows,

$$\begin{aligned}\sum_{e\in\partial\Omega}\int_e \mathbf{F}^N\cdot\mathbf{n}\phi_{i,j}dS = \mathbf{F}^N\left(1,\eta_j\right)\phi_{i,j}\left(1,\eta_j\right)w_j - \mathbf{F}^N\left(-1,\eta_j\right)\phi_{i,j}\left(-1,\eta_j\right)w_j + \\ + \mathbf{F}^N\left(\xi_i,1\right)\phi_{i,j}\left(\xi_i,1\right)w_i - \mathbf{F}^N\left(\xi_i,-1\right)\phi_{i,j}\left(\xi_i,-1\right)w_i\end{aligned} \tag{10}$$

It can be seen that due to the discrete orthogonality of the Lagrange interpolating polynomials, the mass matrix is diagonal, so the inversion is trivial.

The discretisation requires the evaluation of the fluxes along the element edges. Since the grid point values of the solutions are not defined on the edges, the edge values come from evaluating the polynomial representation of the solution. The interpolants from each side differ at the element faces. The difference is resolved by solving a Riemann problem for the flux. Thus,

$$\mathbf{U}^N_{t_{i,j}}w_iw_j + \sum_{e\in\partial\Omega}\int_e \mathbf{F}^{N*}\cdot\mathbf{n}\phi_{i,j}dS - \sum_{\mu,\nu=0}^{N}\mathbf{F}^N_{\mu,\nu}\cdot\nabla\phi_{i,j}w_iw_j = 0 \quad i,j=0,1,\ldots,N \tag{11}$$

where $\mathbf{F}^{N*}$ is the result of solving the Riemann problem. Having obtained a suitable discrete expression for each elemental contribution, it suffices to sum over all elements in the mesh and apply the boundary conditions weakly to finalize the DGSEM method, see details in Kopriva [10]. It is remarkable that when a polynomial of degree $N = 0$ is used, then the classical first order Finite Volume formulation is recovered. It should also be noticed that Eq. 1 does not include non-conservative products. The extension of the DGSEM to include non-conservative products will be performed in Sec. 2.3.

*2.2. **Cell interface flux approximation***

In this section we present the approximate Riemann solvers employed to compute the intercell fluxes $\mathbf{F}^{N*}$ of the 7-equation Baer-Nunziato two-phase flow model.

The Rusanov flux. The Rusanov flux [35, 36] only uses one wave speed S_{max} which is the maximum absolute eigenvalue of left and right states of the Jacobian matrix $\mathbf{A_c}(\mathbf{U})$. The main advantage of the Rusanov flux is its simplicity and low dependence on the eigenstructure of the flux Jacobian. Thus, it is particularly easy to implement when the flux Jacobian is difficult to formulate, for example when a complex equation of state is used. Its main disadvantage is its high diffusion of discontinuities, in particular the contact discontinuities.

The GForce flux. The GForce numerical flux [37, 38] is the weighted average of classical Lax-Wendroff and Lax-Friedrichs fluxes. As the Rusanov flux, the main advantage of the GForce flux is its low dependence on the eigenstructure of the flux Jacobian, only the maximum eigenvalue is required. GForce flux tends to dissipate less than Rusanov flux.

The AUSM+ flux. The AUSM+ flux scheme of Liou [39, 40] has been recently extended to two-phase flows [41, 42]. Its formulation does not depend at all on the hyperbolic nature of the PDE, hence is independent of any flux Jacobian eigenstructure. It is also capable of capturing exactly isolated contact discontinuities.

The VFRoe flux. The VFRoe flux [43, 44, 45] is an approximate Godunov method in the sense that the exact solution to the Riemann problem at the cell interface is replaced by an approximation.

The Godunov flux reads:

$$\mathbf{F}^*(\mathbf{U_L}, \mathbf{U_R}) = \mathbf{F}(\mathbf{U}^*_{ex}(\mathbf{U_L}, \mathbf{U_R}))$$

The key idea of the VFRoe method is to replace the exact solution to the non-linear Riemann problem $\mathbf{U}^*_{ex}(\mathbf{U_L}, \mathbf{U_R})$ by the exact solution to a linearized Riemann problem. The VFRoe scheme will produce entropy-satisfying numerical solutions, if the approximate solution of the Riemann problem is also entropy-satisfying. The approximate Riemann solution for the VFRoe scheme is obtained as in the Roe method. It is well known that it can be entropy-violating. In order to circumvent this issue, locally when $\lambda_i(\mathbf{V_L}) < 0$ and $\lambda_i(\mathbf{V_R}) > 0$, the VFRoe flux is replaced by the Rusanov flux which in turn is entropy-satisfying.

The Osher flux. The main advantage of the Osher flux [46, 47] with respect to the VFRoe scheme is that it does not need any entropy fix. A further advantage of this scheme is that it may be written using a path-conservative formulation, making it particularly suitable to deal with non-conservative products.

The full non-linear flux. The key ingredient is that, given the choice of Baer and Nunziato for the interfacial pressure and velocities, the description of the structure of the exact solution of the Riemann problem is made available. This is possible because away from the linearly degenerate solid contact wave the phases decouple and the equations recover their conservative character.

In other words, it means that away from the solid phase contact discontinuity, the solution of the Riemann problem associated to the mono-phasic Euler equations holds. On either side of the solid contact where α_l is constant, the equations reduce to a pair of Euler equations for each phase separately. Accordingly, the jump conditions across shocks and rarefactions are the same as those for the Euler equations with the chosen equation of state.

The states of the flow to the left (1) and right (2) side of the solid contact are determined completely by the pressures (p_{1_g}, p_{2_g}) of the gas and (p_{1_l}, p_{2_l}) of the liquid. These pressures also determine whether the transitions are shocks or rarefactions, and they specify the positions of these waves. The density ρ_{0_g} of the gas in region 0 (between gas and liquid contact) is the remaining unknown and is obtained through the iterative solution of the thin-layer equations [48, 4].

The HLLC approximation. The HLLC [49] approximation has been extended to the set of Baer-Nunziato equations in [5]. The idea is that instead of performing the analysis of the wave structure (shock or rarefaction waves), which must be carried out on every step of the iterative solution process of the non-linear thin-layer equations, their speed is estimated through HLLC approach. The left and right waves of each phase are treated as discontinuities propagating at approximated speeds.

Then, as it is done for the exact full non-linear flux, the thin layer equations are solved iteratively and all variables in region "0" can be found. Another difference then, with respect to the full non-linear solver is in the construction of the final flux function which follows the HLLC decomposition.

2.3. ***Discretisation of non-conservative terms***

A specificity of the Baer and Nunziato equations is the presence of non-conservative products of the form $\mathbf{H}(\mathbf{U})\frac{\partial \alpha_I}{\partial x}$. The difficulty of integrating this term over a control volume arises in the presence of a discontinuity in the volume fraction.

Our objective in this section is to develop and/or extend discretisation schemes for the non-conservative terms for all numerical fluxes presented in Sec. 2.2 in a Discontinuous Galerkin framework.

In the following, we present two discretisation approaches. The first one is based on physical considerations, in order to recover steady states, the so-called Abgrall criterion. The second approach finds its roots in a recent definition of the product of distributions, following the path-conservative formalism extended here to high order discretisations.

2.3.1. ***Criterion of Abgrall***

One way is to discretise the non-conservative products based on physical considerations. The criterion of Abgrall [50] states that a two-phase flow uniform in velocity and pressure should remain uniform in these variables with time evolution. Applied to the set of Baer and Nunziato equations, this condition can be used to derive a discretisation scheme for the non-conservative terms present in the momentum and energy equations as well as the equation of evolution of the volume fraction. Let us consider three cells of uniform volume Δx indexed by $i-1, i, i+1$, their interfaces by $i-1/2, i+1/2$ and an explicit Euler time discretisation with time-step Δt. Furthermore, let us assume a two-phase flow with constant velocity U and pressure P.

The continuity equation associated to a generic phase of the Baer-Nunziato equation reads:

$$(\alpha\rho)^{(n+1)} = (\alpha\rho)^{(n)} - \frac{\Delta t}{\Delta x}\left(F_{2_{i+1/2}}^{(n)^*} - F_{2_{i-1/2}}^{(n)^*}\right) \tag{12}$$

Denoting by Δ the discrete form of $\frac{\partial \alpha}{\partial x}$ and considering constant pressure and velocity, the momentum equation may be written as:

$$(\alpha\rho)^{(n+1)}U = (\alpha\rho)^{(n)}U - \frac{\Delta t}{\Delta x}\left(F_{3_{i+1/2}}^{(n)^*} - F_{3_{i-1/2}}^{(n)^*}\right) + \Delta t P \Delta \tag{13}$$

Finally the conservation of energy yields to:

$$(\alpha\rho(e+U^2/2))^{(n+1)} = (\alpha\rho(e+U^2/2))^{(n)} - \frac{\Delta t}{\Delta x}\left(F_{4_{i+1/2}}^{(n)^*} - F_{4_{i-1/2}}^{(n)^*}\right) + \Delta t P U \Delta \tag{14}$$

Combining Eqs. 12 and 13, one obtains the following expression for Δ:

$$\Delta = \frac{1}{P\Delta x}\left((F^{(n)^*}_{3_{i+1/2}} - F^{(n)^*}_{3_{i-1/2}}) - U(F^{(n)^*}_{2_{i+1/2}} - F^{(n)^*}_{2_{i-1/2}})\right) \tag{15}$$

If we combine Eqs. 12 and 13 and explicitly use the stiffened gas equation of state, a discretisation of the volume fraction equation may be obtained as:

$$\frac{\alpha^{(n+1)} - \alpha^{(n)}}{\Delta t} = \frac{\gamma - 1}{P + \gamma\pi}\left(\frac{U^2}{2\Delta x}(F^{(n)^*}_{2_{i+1/2}} - F^{(n)^*}_{2_{i-1/2}}) - \frac{1}{\Delta x}(F^{(n)^*}_{4_{i+1/2}} - F^{(n)^*}_{4_{i-1/2}}) + PU\Delta\right) \tag{16}$$

If we apply Eqs. 15 and 16 to the Rusanov scheme, we obtain:

$$\Delta = \frac{-\alpha_{R_{i-1}} - \alpha_{L_i} + \alpha_{R_i} + \alpha_{L_{i+1}}}{2\Delta x} \tag{17}$$

and

$$\begin{aligned}\frac{\alpha^{(n+1)} - \alpha^{(n)}}{\Delta t} = \frac{1}{2\Delta x} \quad & (u_{int}(\alpha_{R_{i-1}} + \alpha_{L_i} - \alpha_{R_i} - \alpha_{L_{i+1}}) \\ & + S_{max_{i-1/2}}(\alpha_{R_{i-1}} - \alpha_{L_i}) \\ & - S_{max_{i+1/2}}(\alpha_{R_i} - \alpha_{L_{i+1}}))\end{aligned} \tag{18}$$

Eqs. 17 and 18 follow the expressions obtained in [2]. If applied to the GForce flux, the expression for Δ remains unchanged, however the discretisation for the volume fraction equation now takes the following form:

$$\begin{aligned}\frac{\alpha^{(n+1)} - \alpha^{(n)}}{\Delta t} = \frac{1}{2CFL_{loc}\Delta x} \quad & (u_{int}CFL_{loc}(\alpha_{R_{i-1}} + \alpha_{L_i} - \alpha_{R_i} - \alpha_{L_{i+1}}) \\ & + (1-\omega)S_{max_{i-1/2}}(\alpha_{R_{i-1}} - \alpha_{L_i}) \\ & - (1-\omega)S_{max_{i+1/2}}(\alpha_{R_i} - \alpha_{L_{i+1}}))\end{aligned} \tag{19}$$

Our objective is to extend these formulations for the Rusanov and GForce fluxes in a Discontinuous Galerkin framework. Integrating the one-dimensional set of Baer and Nunziato equations over a control volume Ω and multiplying by a test function ϕ one obtains:

$$\int_\Omega \frac{\partial \mathbf{U}}{\partial t}\phi dx + \int_\Omega \frac{\partial \mathbf{F}(\mathbf{U})}{\partial x}\phi dx + \int_\Omega \mathbf{H}(\mathbf{U})\frac{\partial \alpha_l}{\partial x}\phi dx = 0 \tag{20}$$

Integrating Eq. 20 by parts yields:

$$\int_\Omega \frac{\partial \mathbf{U}}{\partial t}\phi dx + \left((\mathbf{F}^*_{\mathbf{b}} + \mathbf{H}_{\mathbf{b}}\alpha^*_l)\,\phi\right)|_{\partial\Omega} - \int_{\Omega\setminus\partial\Omega}\mathbf{F}\phi_x dx - \int_{\Omega\setminus\partial\Omega}\frac{\partial \mathbf{H}}{\partial x}\alpha_l\phi dx - \int_{\Omega\setminus\partial\Omega}\mathbf{H}\alpha_l\frac{\partial\phi}{\partial x}dx = 0 \tag{21}$$

We can compare Eq. 21 with Eq. 11 to see that there are two extra terms that require a discretisation: $\mathbf{H}$ and α_l. The discretisation of these terms is performed using Legendre orthogonal polynomials in Lagrange

form (the same discretisation as for the fluxes and the solution, Eq. 5). The integrals are approximated using Legendre-Gauss quadrature, as in the usual DGSEM.

In order to satisfy the criterion of Abgrall for the Rusanov and GForce fluxes, some choices are to be made for the flux $\mathbf{F_b^*}$ and the liquid volume fraction at the interface α_l^*. The classical flux holds the conservative part of the system and is here augmented to hold a contribution from the liquid volume fraction equation, denoted by $F_{1_b}^*$. The schemes are chosen such that:

$$\begin{cases} F_{1_b}^* = -\dfrac{S_{max}}{2}(\alpha_R - \alpha_L) \\ \alpha_l^* = \dfrac{\alpha_R + \alpha_L}{2} \end{cases} \quad \text{for the Rusanov flux} \tag{22}$$

$$\begin{cases} F_{1_b}^* = -\dfrac{S_{max}(1-\omega)}{2CFL_{loc}}(\alpha_R - \alpha_L) \\ \alpha_l^* = \dfrac{\alpha_R + \alpha_L}{2} \end{cases} \quad \text{for the GForce flux} \tag{23}$$

It is easy to check that rewriting Eq. 21 in a Finite Volume way and inserting definitions from Eq.s 22 or 23, one recovers Eqs. 17 to 19. We will see in the results section that these discretisations allow to keep uniformity of the flow even for very high orders.

Developing this strategy for the AUSM+ conservative flux function is however cumbersome due to its formulation. The simplifications of Eqs. 15 and 16 using formal calculus tools did not give satisfactory expressions due to the numerous switches present in the method. Therefore, we adopted the set of conditions from Eq. 22. We will see however that this choice gives very inaccurate results which are independent from the original AUSM+ formulation.

The other schemes detailed in Sec. 2.2, e.g. VFRoe, Osher, the full non-linear flux and its HLLC approximation have their own definitions of $F_{1_b}^*$ and α_l^*. We refer the reader to this section to find references of detailed formulations.

2.3.2. ***Path conservative scheme***

Another approach to treat non-conservative products is based on the theory of Dal Maso *et al.* [51], where they give a definition to a non-conservative product at a discontinuity. By introducing a family of path $\psi : [0,1] \times \mathcal{R}^n \times \mathcal{R}^n$ which satisfy:

$$\psi(0, \mathbf{U_L}, \mathbf{U_R}) = \mathbf{U_L} \text{ and } \psi(1, \mathbf{U_L}, \mathbf{U_R}) = \mathbf{U_R} \tag{24}$$

In Eq.24, $\mathbf{U_L}$ and $\mathbf{U_R}$ represent the left and right states on each side of the contact discontinuity ξ. Then, they define the product at the jump as:

$$\int_{\xi^-}^{\xi^+} \mathbf{H}(\mathbf{U}) \frac{\partial \alpha_l}{\partial x} dx = \int_0^1 \mathbf{H}(\psi(s, \mathbf{U_L}, \mathbf{U_R})) \frac{\partial \psi(s, \mathbf{U_L}, \mathbf{U_R})}{\partial s} ds \tag{25}$$

The simplest path which satisfies 24 is the canonical path $\psi(s, \mathbf{U_L}, \mathbf{U_R}) = \mathbf{U_L} + s(\mathbf{U_R} - \mathbf{U_L})$.

A further step can be taken by rewriting the whole set of non-conservative equations into quasi-linear form (see AppendixA). Then, denoting by $\mathbf{A_c}(\mathbf{U}) = \frac{\partial \mathbf{F}(\mathbf{U})}{\partial \mathbf{U}} + \mathbf{H}(\mathbf{U})\frac{\partial \alpha_l}{\partial \mathbf{U}}$ the extended Jacobian, the full scheme reads:

$$\int_\Omega \frac{\partial \mathbf{U}}{\partial t}\phi dx + \left((\mathbf{U_R}-\mathbf{U_L})\int_0^1 \mathbf{A_c}(\psi(s,\mathbf{U_L},\mathbf{U_R}))\phi ds\right)\Big|_{\partial\Omega} + \int_{\Omega\setminus\partial\Omega}\mathbf{A_c}\frac{\partial \mathbf{U}}{\partial x}dx = 0$$

Integrating by parts the last term, one obtains:

$$\begin{aligned}&\int_\Omega \frac{\partial \mathbf{U}}{\partial t}\phi dx + (\mathbf{F_b}\phi)|_{\partial\Omega} + \left((\mathbf{U_R}-\mathbf{U_L})\int_0^1 \mathbf{A_c}(\psi(s,\mathbf{U_L},\mathbf{U_R}))\phi ds\right)\Big|_{\partial\Omega}\\ &-\int_{\Omega\setminus\partial\Omega}\mathbf{F}\phi_x dx + \left[(\mathbf{H_b}\alpha_l\phi)|_{\partial\Omega} - \int_{\Omega\setminus\partial\Omega}\frac{\partial \mathbf{H}}{\partial x}\alpha_l\phi dx - \int_{\Omega\setminus\partial\Omega}\mathbf{H}\alpha_l\frac{\partial\phi}{\partial x}dx\right] = 0\end{aligned} \tag{26}$$

where $\mathbf{F_b}$ represents the projection of the flux to the face. The final step is obtained by introducing the Godunov state $\mathbf{U}(0)$ in Eq. 26 following [5]:

$$\begin{aligned}&\int_\Omega \frac{\partial \mathbf{U}}{\partial t}\phi dx + (\mathbf{F_b}\phi)|_{\partial\Omega} + (\mathbf{U}_i - \mathbf{U}(0)_{i-1/2})\int_0^1 \mathbf{A_c}(\psi(s,\mathbf{U}(0)_{i-1/2},\mathbf{U}_i))\phi_{i-1/2}ds\\ &+(\mathbf{U}(0)_{i+1/2}-\mathbf{U}_i)\int_0^1 \mathbf{A_c}(\psi(s,\mathbf{U}_i,\mathbf{U}(0)_{i+1/2}))\phi_{i-1/2}ds\\ &-\int_{\Omega\setminus\partial\Omega}\mathbf{F}\phi_x dx + \left[(\mathbf{H_b}\alpha_l\phi)|_{\partial\Omega} - \int_{\Omega\setminus\partial\Omega}\frac{\partial \mathbf{H}}{\partial x}\alpha_l\phi dx - \int_{\Omega\setminus\partial\Omega}\mathbf{H}\alpha_l\frac{\partial\phi}{\partial x}dx\right] = 0\end{aligned} \tag{27}$$

The discretisation of $\mathbf{H}$ and α_l is performed using Legendre orthogonal polynomials in Lagrange form while the integrals may be approximated using for example Legendre-Gauss quadrature. Note that if a polynomial order of degree $N = 0$ is used, then the solution is constant inside the cell and $\mathbf{F_b}$ together with the third line of Eq. 27 cancel out yielding a classical Finite Volume formulation. This approach has been adopted to extend the VFRoe, full non-linear flux and its HLLC approximation. The Osher flux already uses this formalism (see [46, 47]).

2.4. ***Stabilisation using an artificial viscosity method***

All upwind schemes presented earlier may yield high oscillations in the vicinity of discontinuities. Classical limiters work well in order to avoid the local creation of extrema, however they severely degrade the accuracy, often reduced to one in the entire cell. In this work, we follow an artificial viscosity approach [11]. The idea of the artificial viscosity is to add a controlled amount of viscosity to the governing equations in the vicinity of strong gradients, such as shock waves or contact discontinuities. In this way the discontinuity may be resolved in the space of interpolating polynomials. The new set of equations reads:

$$\frac{\partial \mathbf{U}}{\partial t} + \frac{\partial \mathbf{F}}{\partial x} + \mathbf{H}\frac{\partial \alpha_l}{\partial x} = \frac{\partial}{\partial x}\left(\epsilon\frac{\partial \mathbf{U}}{\partial x}\right) \tag{28}$$

Then the discontinuity should spread over a layer of thickness ϵ. The definition of the parameter ϵ that controls the amount of viscosity introduced as well as the definition of a sensor to capture the regions where the stabilising viscosity should be added are key aspects in the development of the artificial viscosity method.

The discontinuity sensor is built following [11]. Spectral methods represent the solution of the problem as a sum of basis functions multiplied by some coefficients. In particular the DGSEM uses the Legendre orthogonal polynomials as a basis and therefore a one dimensional solution of order N, can be represented in each element as

$$\mathbf{U}^N(x) = \sum_{i=0}^{N} \tilde{\mathbf{U}}_i^N L_i(x), \tag{29}$$

where $\tilde{\mathbf{U}}_i^N$ is the projection of the solution onto the basis function $L_i(x)$, that is a Legendre orthogonal polynomial. It should be noticed that the DGSEM is a nodal method, and therefore the coefficients obtained in Eq. 11 are not directly $\tilde{\mathbf{U}}_i^N$. However, they can be computed from the nodal values as

$$\mathcal{V}\tilde{\mathbf{U}}^N = \mathbf{U}^N, \tag{30}$$

where matrix $\mathcal{V}$ is a Vandermonde matrix [52]. A particularity of spectral methods is that for smooth solutions the coefficients $\tilde{\mathbf{U}}_i$ decay very quickly (exponential convergence), while the convergence rate is poor (algebraic convergence) for non smooth solutions [16].

A truncated expansion of order $N-1$ of the solution, $\mathbf{U}^N(x)$, is also constructed as

$$\hat{\mathbf{U}}^{N-1}(x) = \sum_{i=0}^{N-1} \tilde{\mathbf{U}}_i^N L_i(x). \tag{31}$$

The difference between the truncated expansion of the solution, $\hat{\mathbf{U}}^{N-1}$, and the solution itself, $\mathbf{U}^N$, is small for smooth solutions and big for discontinuous solutions due to spectral convergence. In order to measure the difference between the two functions the following indicator is computed within each element:

$$s = \log_{10} \max \left(\frac{(\mathbf{U}^N - \hat{\mathbf{U}}^{N-1}, \mathbf{U}^N - \hat{\mathbf{U}}^{N-1})}{(\mathbf{U}^N, \mathbf{U}^N)} \right) \tag{32}$$

where $(u, v) = \int_{-1}^{1} uvdx$ represents the usual L^2 inner product and can be approximated using Legendre-Gauss quadrature. It should be noticed that the maximum value among all the equations is taken, which is justified as the objective of the indicator is to capture discontinuities in any of the equations.

Finally, ϵ, the amount of viscosity imposed in each element, is computed as:

$$\epsilon = \begin{cases} 0 & \text{if } s < s_0 - \kappa \\ \dfrac{\epsilon_0}{2}\left(1 + \sin \dfrac{\pi(s - s_0)}{2\kappa}\right) & \text{if } s_0 - \kappa \leq s \leq s_0 + \kappa \\ \epsilon_0 & \text{if } s > s_0 + \kappa \end{cases} \tag{33}$$

In this work, the values of $\epsilon_0 = \frac{h}{(N+1)}$ (being h the size of the elements), $s_0 = \log_{10} \frac{1}{(N+1)^4}$ and $\kappa = 5$ were chosen empirically and demonstrated very satisfactory results. As it is explained in [11], the selection of these values for the parameters introduces viscosity only when the solution is not continuous and the profiles of the

discontinuities are sharp but smooth. The effectiveness of these parameters to correctly capture the discontinuities and stabilise the solution will be studied in Sec. 4.3.

The artificial viscosity method produces an *a posteriori* stabilisation, i.e. the solution is not stabilised until the oscillation is generated. In general there is no problem with this, however if the amplitude of the oscillation is too high it can transiently produce unphysical values of the variables, e.g. negative densities or volume fractions outside the interval $[0, 1]$. This in inadmissible as the computation of some quantities, e.g. the speed of sound, would result in invalid operations. The development of a robust artificial viscosity method requires the introduction of relaxation iterations. If any of the aforementioned variables acquire an unphysical value as a result of an oscillation, a relaxation iteration is performed instead of the regular iteration. In a regular iteration, the time derivative of the solution is computed as

$$\frac{\partial \mathbf{U}}{\partial t} = -\frac{\partial \mathbf{F}}{\partial x} - \mathbf{H}\frac{\partial \alpha_l}{\partial x} + \frac{\partial}{\partial x}\left(\epsilon \frac{\partial \mathbf{U}}{\partial x}\right), \tag{34}$$

while in a relaxation iteration, only the diffusive terms are computed

$$\frac{\partial \mathbf{U}}{\partial t} = \frac{\partial}{\partial x}\left(\epsilon \frac{\partial \mathbf{U}}{\partial x}\right). \tag{35}$$

It should be noticed that relaxation iterations do not produce an advance in physical time but only a filtering of the solution. As will be seen in Sec. 4.3, relaxation iterations are only activated in particular test cases.

The derivation of the DGSEM performed in Sec. 2.1 does not include second order derivatives. Several methods are available in the literature to perform the discretisation of elliptic problems, e.g. Bassi-Rebay 1 [53], Local Discontinuous Galerkin [54], Compact Discontinuous Galerkin [55] or Symmetric Interior Penalty Discontinuous Galerkin [56]. A thorough review of all these methods within a unified framework can be found in [57].

In this work, we will compare the efficiency for the artificial viscosity method of the Bassi-Rebay 1 (BR1) and the Symmetric Interior Penalty (SIP) implementations. The main advantage of the BR1 method is that it is easy to implement. The disadvantages of the BR1 method are that the resultant scheme is non compact (the approximation in one element depends on the solution in non neighbor elements) and only weakly stable (understanding stability as ensuring that the numerical model enjoys the same solution uniqueness as the analytical solution of the mathematical model)[57]. The non compactness of the scheme is especially critical for implicit solvers, where the Jacobian couples the non neighbor elements. However, BR1 works well for explicit computations for advection dominated equations. As far as the Symmetric Interior Penalty method is concerned, it results in a compact and stable scheme. Its main disadvantage is that it includes a penalty parameter that guarantees the stability for a high enough value but also produces stiffness. A formula to compute a value of the penalty parameter that keeps the stability was derived in [58] and simplified in [59]. This formula is applied here to compute the penalty parameter. The efficiency of BR1 and SIP for the artificial viscosity method will be tested in Sec. 4.3.

3. First order results

In this section, our aim is to make a serie of comparisons between all upwind schemes presented in Sec. 2.2. Several shock tube problems are used to test the capturing properties of the different flux schemes in the presence of discontinuities.

We consider seven test problems which are classical benchmark, see for instance [5]. The initial data consists of two constant states separated by a discontinuity located at $x = x_0$, all the parameters are listed in Tables 1-3. Transmissive boundary conditions are imposed at $x = 0$ and $x = 1$. All the results presented below were computed on a mesh of 100 elements, except for test 6 where an additional 500 elements mesh is used. A comparison is made between all Riemann solvers presented in Sec. 2.2 for a first-order discretisation (which corresponds to a classical Finite Volume approach), results are shown in Figs. 2 and 3 where the mixture density is displayed ($\rho_m = \alpha_l\rho_l + \alpha_g\rho_g$). Final time has been set to $t = 0.2$ for test 0, $t = 0.15$ for tests 1 to 5 and $t = 0.006$ for test 6.

	Test 0	Test 1	Test 2	Test 3	Test 4	Test 5	Test 6
γ_l	1.4	1.4	3.0	1.4	1.4	3.0	3.0
γ_g	1.4	1.4	1.35	1.4	1.4	1.4	1.4
π_l	0.0	0.0	3400.0	0.0	0.0	10.0	100.0
π_g	0.0	0.0	0.0	0.0	0.0	0.0	0.0
x_0	0.5	0.5	0.5	0.5	0.5	0.5	0.8

Table 1: One-dimensional shock tubes. EOS parameters and initial discontinuity position.

Test	α_{L_l}	ρ_{L_l}	u_{L_l}	p_{L_l}	α_{R_l}	ρ_{R_l}	u_{R_l}	p_{R_l}
0	0.5	1.0	0.0	1.0	0.5	0.125	0.0	0.1
1	0.8	1.0	0.0	1.0	0.3	1.0	0.0	1.0
2	0.2	1900.0	0.0	10.0	0.9	1950.0	0.0	1000.0
3	0.8	1.0	0.75	1.0	0.3	0.125	0.0	0.1
4	0.8	1.0	-2.0	0.4	0.5	1.0	2.0	0.4
5	0.6	1.4	0.0	2.0	0.3	1.0	0.0	3.0
6	0.7	1.0	-19.5975	1000	0.2	1.0	-195975	0.01

Table 2: One-dimensional shock tubes. Initial data for the liquid phase.

Test 0. This preliminary test considers a constant volume fraction in all the domain. In this situation, both phases are fully decoupled as the interfacial terms vanish. This test case is well known as Sod shock tube [60]. The obtained results naturally follow those present in the literature. An important aspect of this test case for the Baer and Nunziato set of equations is the expected ability of the path-conservative schemes to recover exactly the flux formulation for conservative systems. However, as can be seen in Fig. 1, differences are observable for

Test	α_{L_g}	ρ_{L_g}	u_{L_g}	p_{L_g}	α_{R_g}	ρ_{R_g}	u_{R_g}	p_{R_g}
0	0.5	1.0	0.0	1.0	0.5	0.125	0.0	0.1
1	0.2	0.2	0.0	0.3	0.7	1.0	0.0	1.0
2	0.8	2.0	0.0	3.0	0.1	1.0	0.0	1.0
3	0.2	1.0	0.75	1.0	0.7	0.125	0.0	0.1
4	0.2	1.0	-2.0	0.4	0.5	1.0	2.0	0.4
5	0.4	1.4	0.0	1.0	0.7	1.0	0.0	1.0
6	0.3	1.0	-19.5975	1000.0	0.8	1.0	-19.5975	0.01

Table 3: One-dimensional shock tubes. Initial data for the gas phase.

the VFRoe/VFRoePC and the HLLC/HLLCPC. These differences are in agreement with the tests performed by Abgrall et al. [61] where they compared a path-conservative Roe scheme on Euler equations written in non-conservative form (primitive variables) to the classical Roe flux in conservative form. A mesh refinement study tends to decrease these differences as well as the use of a less dissipative scheme. Indeed, the full non-linear flux give more accurate results and a better agreement with its path-conservative version.

Test 1. The liquid phase wave pattern consists of a left rarefaction, a right shock wave and a right travelling liquid contact, while the gas phase consists of a left rarefaction, a contact and a right shock wave. The equations of state for both phases are assumed ideal, with $\gamma_g = \gamma_l = 1.4$. In this test case, the Rusanov, GForce and AUSM+ fail to predict correctly the liquid contact. Furthermore, the AUSM+ scheme gives very inaccurate results, due to the discretisation of non-conservative terms. Remind that the schemes adopted for the non-conservative terms are the same as those developed for the Rusanov flux. Clearly, this assumption cannot be made and show how dependent is the discretisation of non-conservative products on the full scheme. A full development of a compatible non-conservative discretisation for the AUSM+ would be necessary but is beyond the scope of this work. From now on, AUSM+ will be skipped from the comparative study. All other Riemann solvers behave generally much better. Here, the full non-linear Riemann solver and its HLLC approximation are undistinguishable.

Test 2. This test problem is more demanding than Test 1 as it includes large variations of initial data and non-ideal equation of state. As far as the other Riemann solvers are concerned, the same remarks as in Test 1 hold. Rusanov and GForce fluxes suffer from a high dissipation with respect to more accurate schemes.

Test 3. The solution, for both phases, consists of a right shock wave, a right travelling contact discontinuity and a left sonic rarefaction wave. The correct resolution of the sonic point is very important in assessing the entropy satisfaction property of the numerical scheme. With the exception of the very diffusive Rusanov and GForce fluxes, all the other present a non-physical entropy glitch at the sonic point, but it can be checked that it slowly vanishes when the mesh is refined. The path-conservative approach tends to amplify this phenomenon. It can be noticed that the simple entropy fix in the VFRoe scheme (local Rusanov flux), while not perfect, gives

satisfactory results. In particular the path-conservative formalism applied to the VFRoe scheme give very close results to the Osher flux, which in turn is entropy satisfying.

Test 4. Both solid and gas phases consist of a two symmetric rarefaction waves and a trivial stationary contact wave. The region between the rarefaction waves is close to vacuum, therefore this test case is useful to assess the pressure positivity in different numerical methods. In this test case we were unable to make the path-conservative schemes work, as the pressure and density approached zero, positivity preserving was lost for any CFL. The non-linear Riemann solver and its HLLC approximation are clearly superior here and the other schemes give comparable results.

Test 5. This test was designed to assess the ability of numerical methods to resolve the stationary isolated contact waves. The exact solution allows the existence of the stationary contact waves in the solid and gaseous phases when the volume fraction and solid pressure gradients are present across the solid contact. The solution of this test problem contains isolated contacts in both solid and gas phases. As far as the other approaches are concerned, it can be seen that except the Rusanov and GForce schemes, all other allow to resolve exactly the isolated contact waves.

Test 6. This test is a strong-shock test problem, which was designed to assess the robustness and accuracy of numerical methods. The solution of this problem contains, for each phase, a right travelling shock wave, a contact discontinuity and a left rarefaction wave. As the jump of initial pressures is very large, strong shock waves are generated in each phase; the distance between the right shock and contact waves is small in the gas phase (see Fig. 4(d)). These flow features can lead to inaccuracies in numerical solution. We were unable to perform this test case using the path-conservative formalism applied to the HLLC solver. As reported in [5], a fine tuning of the initial guess for the solution of the non-linear thin layer equations was necessary. Apart from the Rusanov and GForce schemes which gave slightly worse results, all Riemann solvers behaved in a comparable way. A comparative test on a refined grid with 500 elements (ensuring about 10 cells between the contact and the shock in the gas phase) is displayed in Figs. 4 and reveals oscillations in the path-conservative VFRoe scheme. In fact, on even finer grids the VFRoe starts to oscillate as well. Also, the HLLC approximation scheme of Tokareva and Toro [5] diverges for any CFL on a grid of 1000 elements. On such fine grids, only the most dissipative Rusanov and GForce and the complete Riemann solvers of Osher and the full non-linear flux behave well and give a stable shocked state.

Given the results of these seven test cases, it is clear that the flux discretisation has a great impact on the overall accuracy and detection of flow features. It is clear that on coarse meshes and with a low-order approach, the Rusanov and GForce schemes give quite inaccurate results, however proved to be very robust as they produced results on every test case. The most accurate results were provided by the full non-linear Riemann solver and its HLLC approximation. However, at a much higher computational cost, because a system of four non-linear equations (the thin layer equations) must be resolved at each edge of the mesh and at each time step. Applied on a multidimensional problem this can be an unrealistic expense. In these one dimensional problems the computational time required by the Rusanov flux was about 20% of the time required by the

full non-linear solver, time computed for a whole flow simulation (Test 1). Under these conditions, the VFRoe scheme seems to be a very good candidate, as it gave accurate results and implied a time overhead of about 15% with respect to the Rusanov flux.

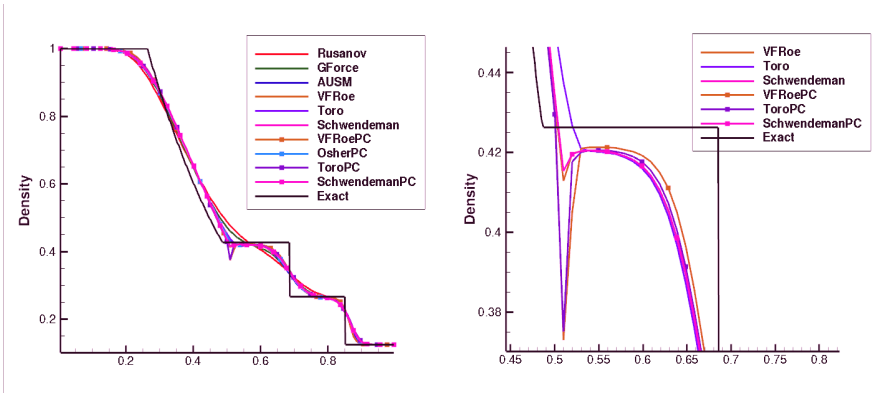

(a) (b)

Figure 1: Shock tube problems. Test 0, density. First order comparison of upwind solvers using 100 elements. (a): all fluxes and (b): magnified view of path-conservative schemes.

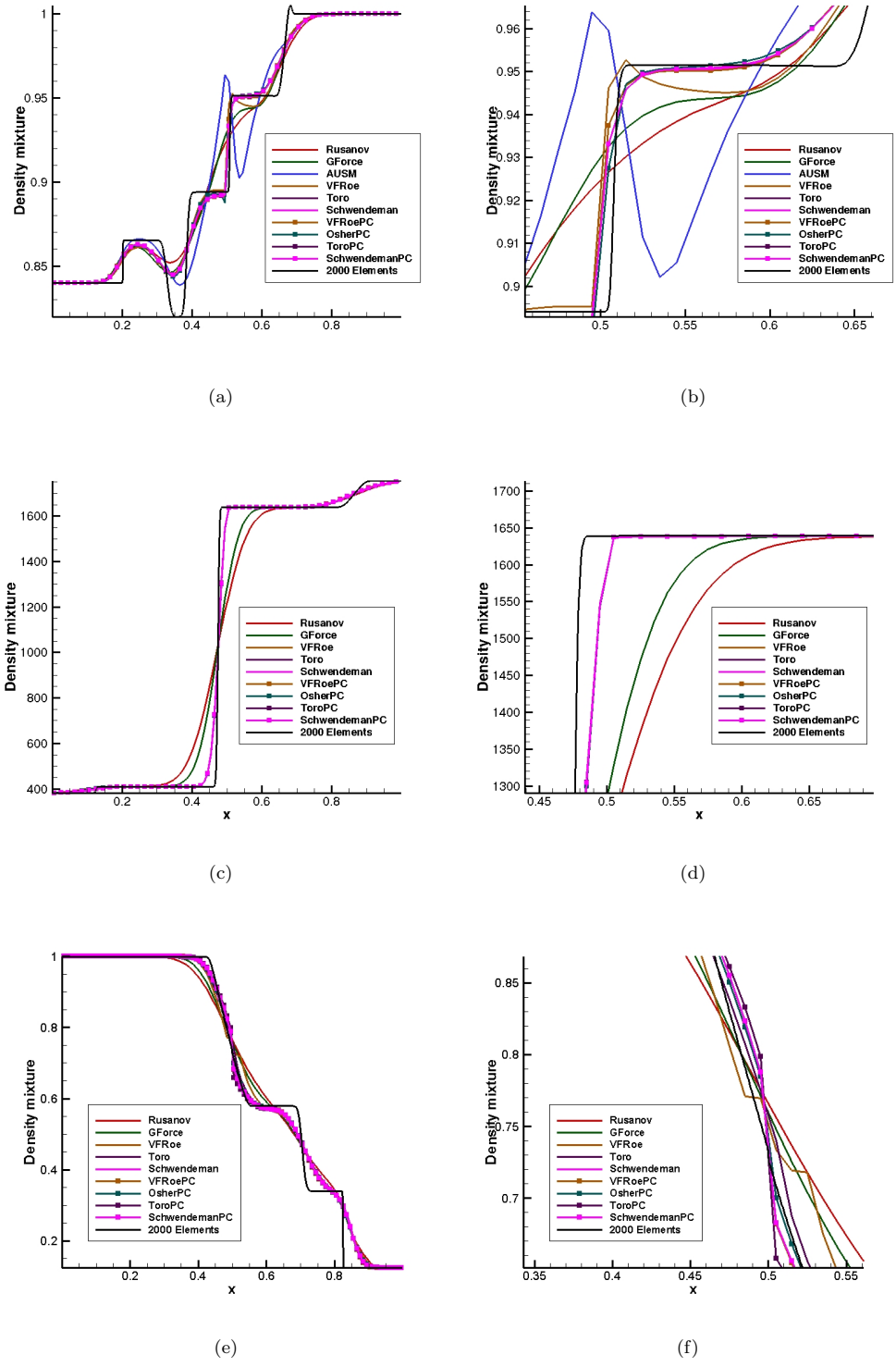

Figure 2: Shock tube problems. Tests 1 to 3. First order comparison of upwind solvers using 100 elements. Density mixture, right column is a specific zoomed region.

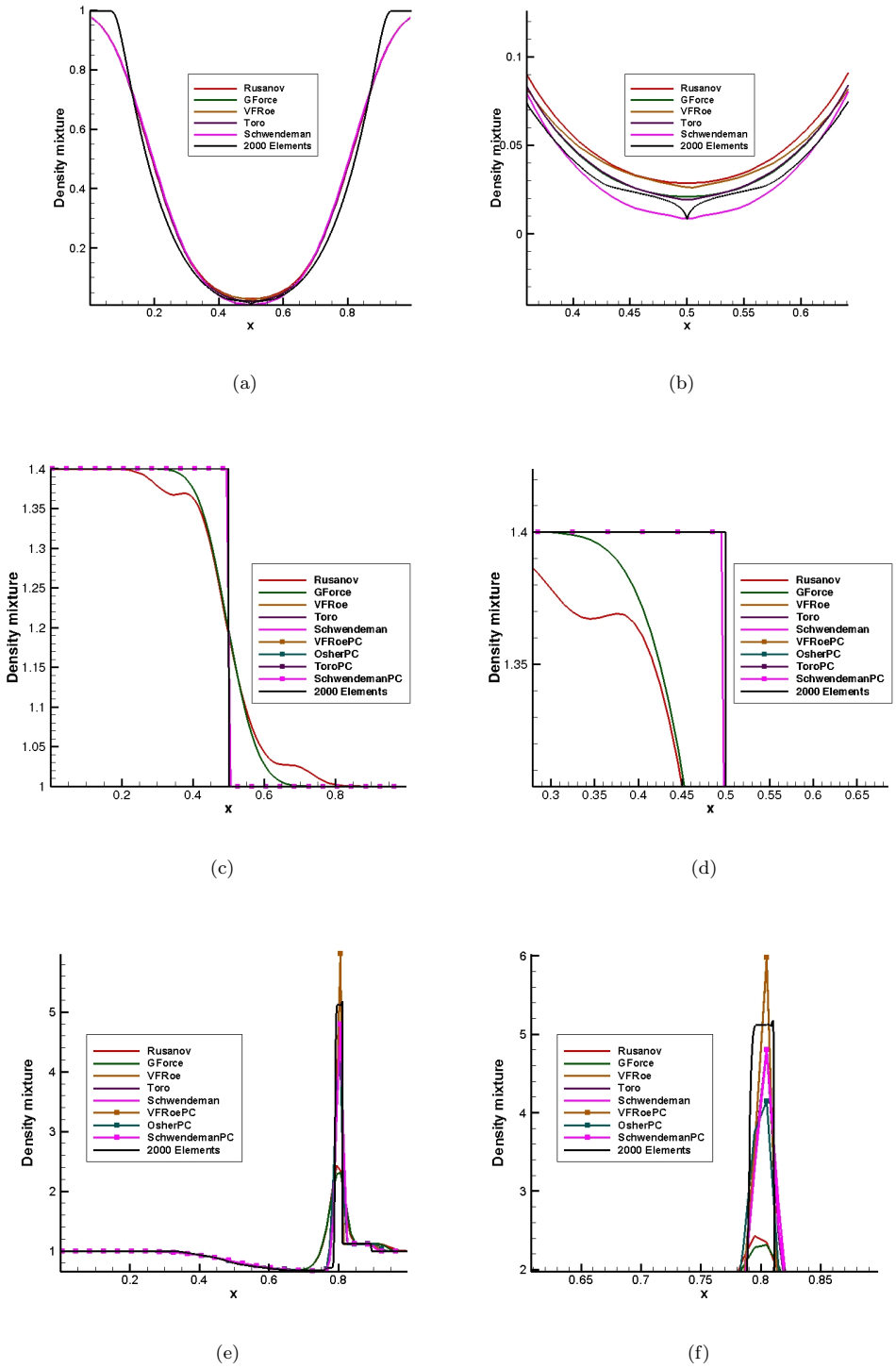

Figure 3: Shock tube problems. Tests 4 to 6. First order comparison of upwind solvers using 100 elements. Density mixture, right column is a specific zoomed region.

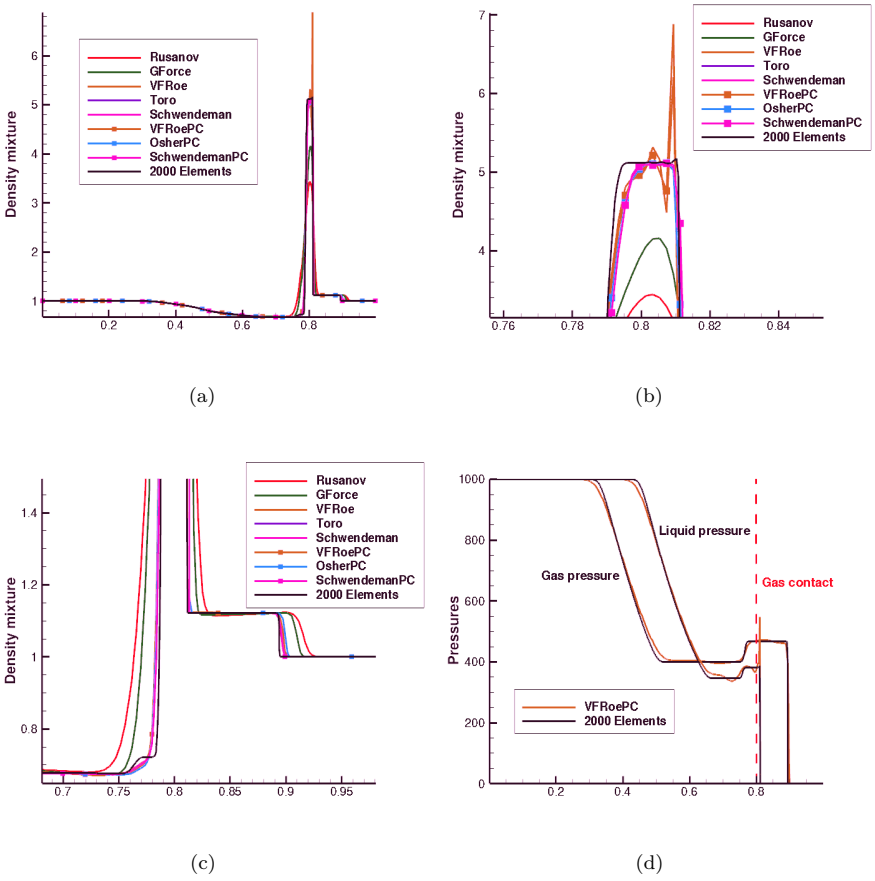

Figure 4: Shock tube problems. Test 6 on a finer grid. First order comparison of upwind solvers using 500 elements. Density mixture, whole domain and specific zoomed regions.

4. Extension to higher order

Discontinuous Galerkin methods naturally allow to construct a high-order solution. However, in the presence of discontinuities special care has to be taken in order to avoid destructive oscillations. In this section, we propose two strategies to evaluate the high-order non-conservative products and a simple method to stabilize oscillations in the vicinity of discontinuities. Then, the approach retained is tested on one-dimensional shock-tube cases. Finally a comparison is performed in a two-dimensional framework with a classical TVD-MUSCL Finite Volume reconstruction.

4.1. ***High-order comparison between Rusanov, VFRoe and path-conservative VFRoe schemes***

As we have seen in Sec. 3, when the spatial discretisation uses a first order representation of the solution, the Rusanov flux, although robust, does not give satisfactory results in the sense that it dissipates too much discontinuities. Here, we propose to apply the concept of artificial viscosity presented in Sec. 2.4 to the Rusanov, VFRoe and path-conservative VFRoe fluxes. A comparison is made between these schemes using a first order discretisation and using a fifth order polynomial reconstruction, on a mesh consisting of 100 elements. In order to stabilize the oscillations which typically occur when a method tries to interpolate through a discontinuity, the artificial viscosity approach detailed in Sec. 2.4 is employed. Several tests are performed using Test 1 to Test 5 and compared using a first order full non-linear Riemann solver on a mesh consisting of 2000 elements, results are displayed in Fig. 5. The results and conclusions differ greatly from the low-order comparison of section Sec. 3. While in a low-order framework, huge differences in accuracy were observable between the Rusanov and the VFRoe flux, or more accurate Riemann solvers, when the order of the spatial discretisation increases, these differences become very low. In all test cases presented here, the fifth order curves of Rusanov, VFRoe and path-conservative VFRoe are almost undistinguishable. It is remarkable how the artificial viscosity approach achieves to impose a very controlled amount of viscosity, keeping very sharp fronts and almost no oscillations.

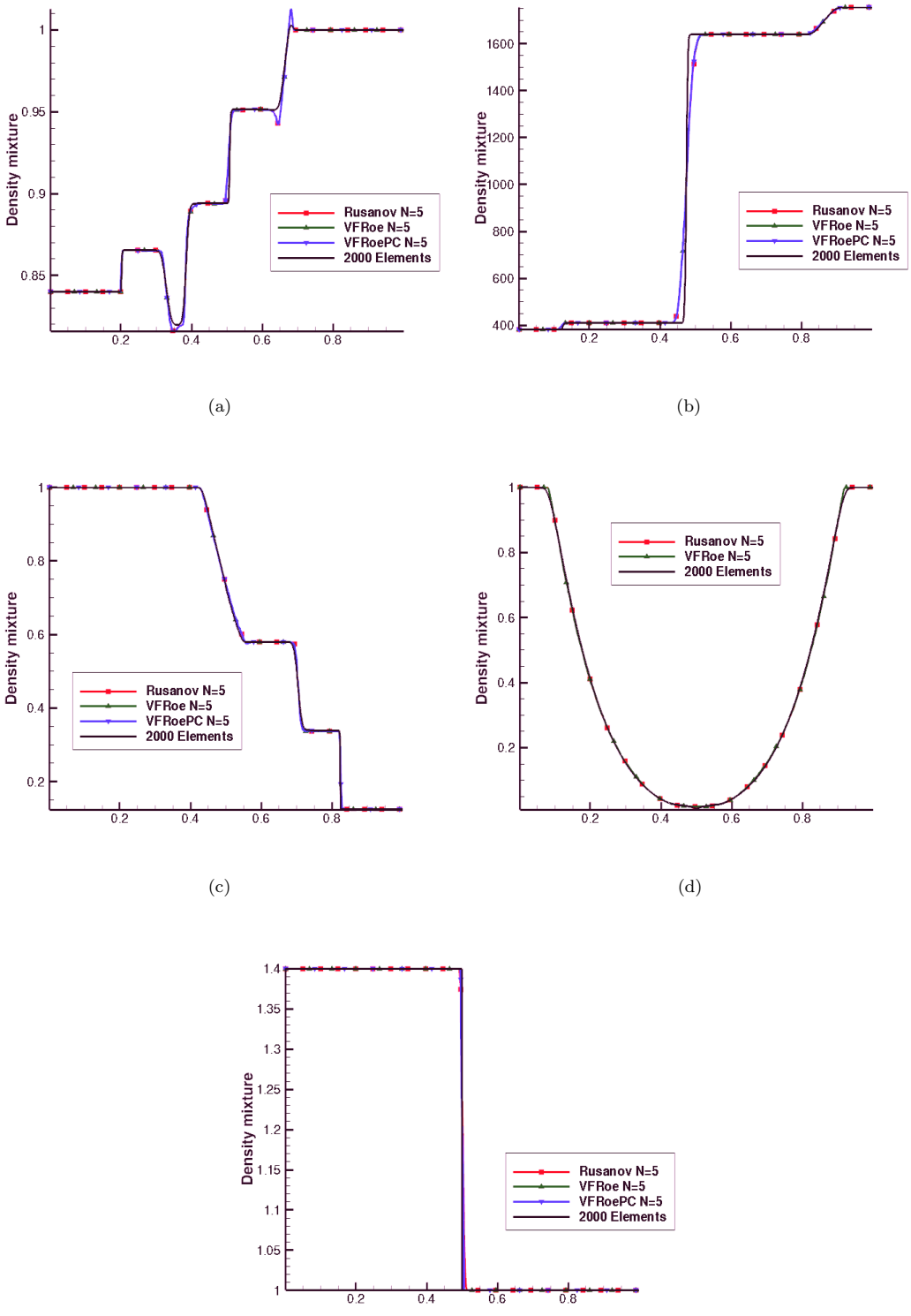

Figure 5: Shock tube problems. Tests 1 to 5. Comparison between Rusanov and VFRoe numerical flux using a fifth order polynomial and 100 elements. Density mixture.

4.2. ***Volume fraction discontinuity in a uniform flow***

A crucial requirement of the non-conservative terms is that their discretisation allow a flow initially at constant pressure and velocity to stay unperturbed by the presence of a volume fraction discontinuity. Our Rusanov and GForce non-conservative fluxes have been built upon this condition, and we will check here that it is verified even for very high orders stabilised by artificial viscosity. A domain of 1 m length is considered. A layer of water initially located in $x \in (0.2, 0.3)$, with volume fraction $\alpha_l = 0.99$ and stiffened gas equation of state parameters $\gamma_l = 4.4, P_\infty = 6.8 \times 10^8$, is set in motion in a uniform flow at atmospheric pressure and constant velocity $v = 100$ m.s^{-1}. The rest of the domain is filled with air modeled as a perfect gas with volume fraction $\alpha_g = 0.99$. Results are displayed after a physical time of 3.10^{-3} s in Fig. 6. A comparison is shown between a zeroth-order polynomial solution on a mesh composed of 600 elements and fifth-order polynomial solutions on 100 elements. High-order Rusanov, GForce, VFRoe and path-conservative VFRoe are displayed and demonstrate equivalent accuracy. Most importantly, it is clear that the uniformity of the flow is perfectly maintained for all schemes.

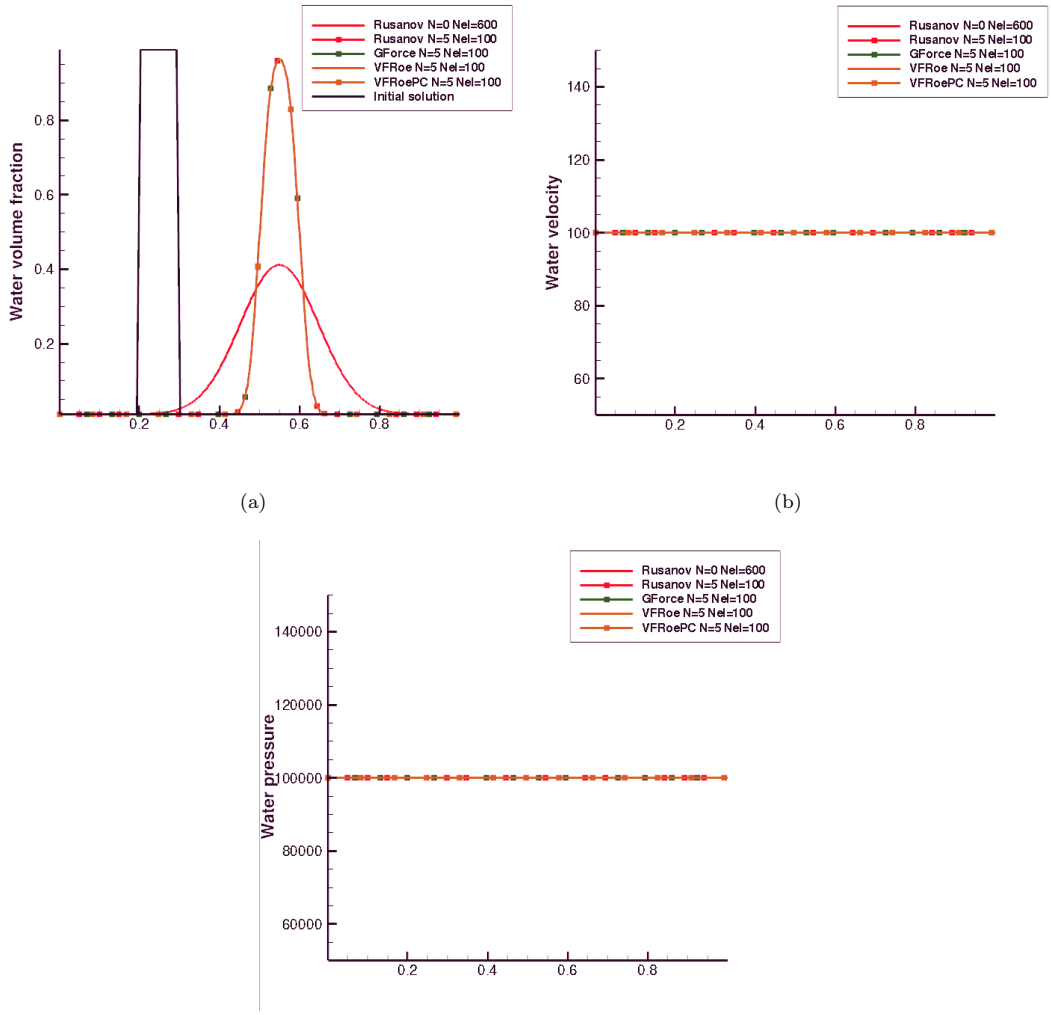

Figure 6: Advection of a volume fraction discontinuity in a uniform flow. (a): Water volume fraction, (b): water velocity and (c): water pressure.

4.3. ***Stabilisation using artificial viscosity method***

The stabilisation method introduced in Sec. 2.4 will be tested in this section. The analysis will focus on the discretisation method for the second order derivatives, i.e. Bassi-Rebay 1 (BR1) and Symmetric Interior Penalty (SIP), and the amount of viscosity used in the stabilisation process. Besides, special attention will be paid to the extra iterations introduced by the stabilisation method. All the test cases in this section make use of the high-order Rusanov non-conservative flux described before.

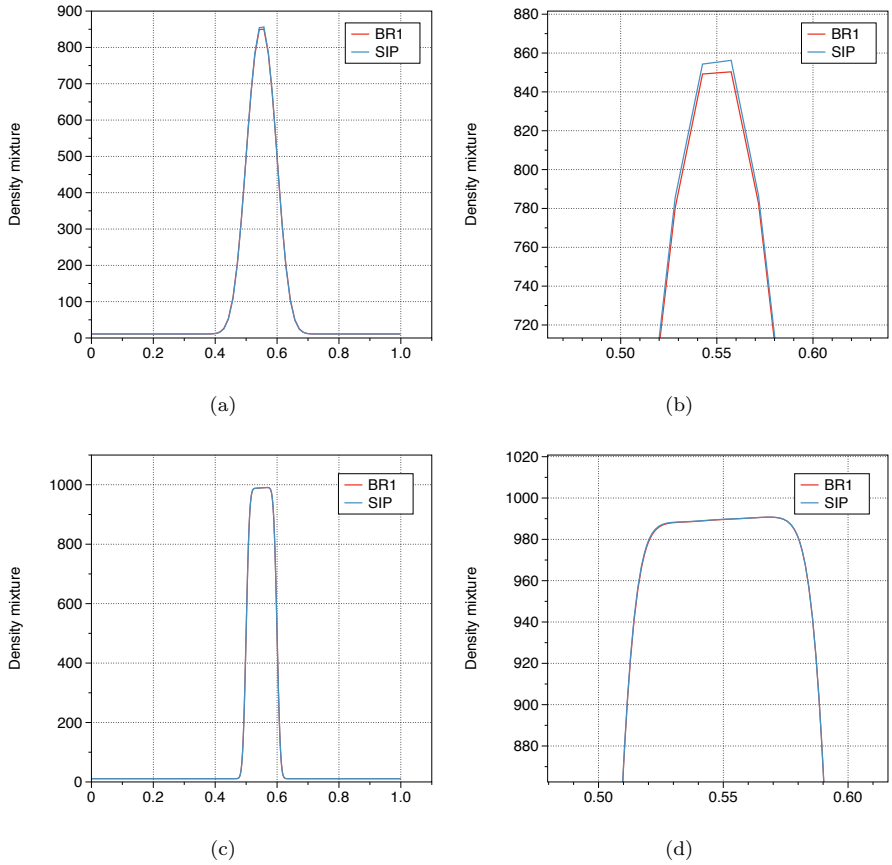

Figure 7: Droplet advection results. Comparison of SIP and BR1 implementations for the artificial viscosity.

First we present a test case where the BR1 and the SIP implementations are compared. Figure 7 shows density mixture plots for the advection problem of Sec. 4.2 at time $t = 0.003$ s with the same parameters and initial conditions. The first test case (a) and (b) shows the solution obtained with 20 elements and polynomial order $N = 9$ while the second (c) and (d) shows the solution obtained with 100 elements and polynomial order $N = 9$. It can be seen that SIP implementation gives a solution with slightly smaller dissipation. In this case, the stabilisation method introduces extra iterations when unphysical values are obtained. In particular, oscillations due to the discontinuous initial solution yield values of the volume fraction higher than 1 and smaller than 0. In the first test case (a) and (b) the amount of extra iterations is about 45% for the SIP and 48% for the BR1. For the second test case (c) and (d) the amount of extra iterations is about 23% for the SIP and 25%

for the BR1. This may be explained by the weakly stable nature of the BR1 implementation and justifies the selection of the SIP as the discretisation method for our artificial viscosity method.

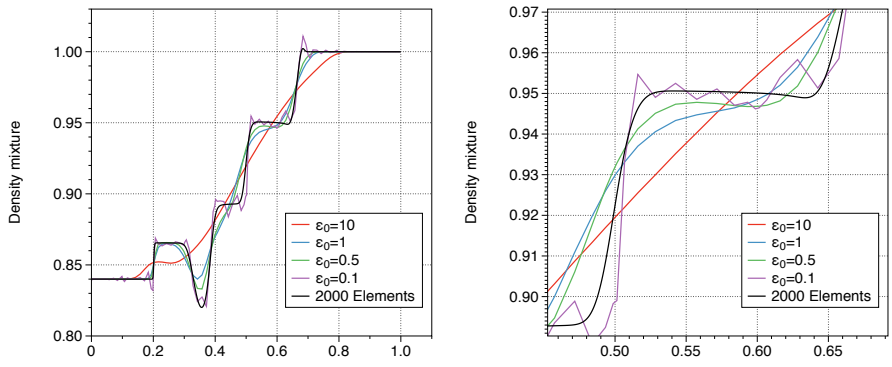

(a) (b)

Figure 8: Test 1 results. Effect of ϵ_0 value in the stabilisation of the solution through the artificial viscosity method.

As far as the amount of viscosity introduced is concerned, we solve Test 1 introduced in Sec. 3 with different values of the parameter ϵ. The results can be seen in Figure 8. In particular, we change the value of ϵ_0 from its definition in Sec. 2.4. Remind that it was defined as $\epsilon_0 = \frac{h}{N+1}$. Here we change its value multiplying it by 10, 1, 0.1 and finally 0.5. A solution obtained with first order and 2000 elements is also plotted for comparison. On the one hand, it can be seen that if the amount of viscosity introduced is higher than the reference value ($\epsilon_0 = 10\frac{h}{N+1}$) the diffusion is higher than necessary. On the other hand, if the diffusion is smaller ($\epsilon_0 = 0.1\frac{h}{N+1}$) not enough diffusion is introduced resulting in undesirable oscillations. The chosen value of $\epsilon_0 = \frac{h}{N+1}$ gives satisfactory results although a better result is obtained with $\epsilon_0 = 0.5\frac{h}{N+1}$. This means that although the chosen value for the parameter gives accurate solutions, even more accurate results can be obtained by tuning the parameter around this value. Finally, it should be noticed that in this case, no extra iterations where required by the method.

4.4. ***Two-dimensional test cases and comparison with TVD-MUSCL Finite Volume reconstruction***

While the above comparisons and developments were presented in one-dimension for the sake of clarity, the extension to multidimensional problems does not pose further difficulties, given that applying the divergence theorem to the governing equations, the Riemann problem is solved in the normal direction to an edge. In the following we will then test our artificial viscosity Discontinuous Galerkin approach on two-dimensional test cases.

The first test is concerned with spectral convergence using a smooth solution, to ensure that the artificial viscosity method does not activate away from discontinuities. Then a comparison with classical Finite Volume solution reconstruction is presented to assess the gain per degree of freedom obtained using high-order Discontinuous Galerkin.

4.4.1. ***Numerical convergence study***

In order to verify the accuracy of the discretisation, the Method of Manufactured Solutions [62] is used. This method is employed extensively in the context of CFD code verification. It consists in defining an analytic solution, and modifying the governing equations accordingly, by adding a source term S. This source term S is added such that the chosen analytic solution satisfies the governing equations.

In the code verification step, when systematic mesh or order refinement studies are performed to examine the accuracy, it is important that the analytic solution employed fulfils some requirements. Although the form of the manufactured solution is somewhat arbitrary, it should be chosen to be smooth, infinitely differentiable (to avoid the cancelation of higher order derivatives) and realisable (i.e., solutions should be avoided that have negative densities, pressures, temperatures and volume fraction strictly bounded between 0 and 1). The solution chosen in the scope of this work is as follows:

$$\begin{cases} \alpha_l = \dfrac{9}{10} - \dfrac{1}{2}\cos(xy) \\ \rho_l = 1 + \cos(xy) \\ u_l = \dfrac{2 + \cos(2x) - \sin(3y)}{10} \\ v_l = \dfrac{2 + \cos(2x) + \sin(3y)}{12} \\ p_l = 1 + \cos(x) + \sin(y) \\ \rho_g = 1 + \cos(2xy) \\ u_g = \dfrac{2 + \cos(4x) - \sin(6y)}{10} \\ v_g = \dfrac{2 + \cos(4x) + \sin(6y)}{12} \\ p_g = 1 + \cos(2x) + \sin(y) \end{cases}$$

In order to assess the accuracy of the discretisation of the 7-equation model using a Discontinuous Galerkin approach, the exact solution is compared to the numerical one using different number of elements or different polynomial orders. In all cases the GForce approximate Riemann solver has been used. The L_∞ norm of the discretisation error (difference between exact and approximate solution) for all conservative variables is computed and reported in Fig.9(a) for an h-refinement study (fixed polynomial order and varying number of elements) and in Fig.9(b) for a p-refinement study (fixed number of elements and varying polynomial order). With a third order polynomial, a fourth order accurate spatial discretisation method is obtained. When the number of elements is kept constant and the polynomial order changes, a law of the type $\sim CN^{-N}$ is recovered, thus the convergence is spectral which is the desired result. It is of importance because it demonstrates the ability of the artifical viscosity method to deal with smooth regions and to maintain convergence to steady states. Classical limiters used in the Finite Volume community sometimes suffer from loss of accuracy away from discontinuities and convergence issues when they are not differentiable (minmod limiter for instance).

4.4.2. ***Two-dimensional Riemann problems***

In order to compare our high-order approach to more classical methods, we employed a well-known strategy in the Finite Volume community: a solution reconstruction based on MUSCL approach. Its extension to the set

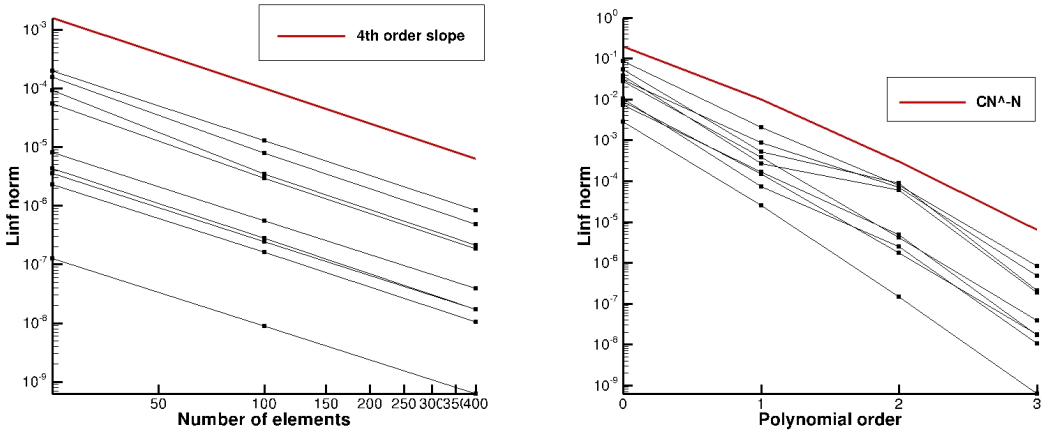

(a) (b)

Figure 9: Two-dimensional manufactured solution. $||.||_{L_\infty}$ of the discretisation error for all conservative variables. (a): h-refinement from 25 to 400 elements, 3rd order polynomial and (b): p-refinement from 0th to 3rd order polynomial, 400 elements.

of Baer-Nunziato equations is for instance presented in [4]. In this approach, the left and right states at an edge are corrected using a *minmod* slope-limited reconstruction. The corrections are obtained in terms of primitive variables. Denoting by $+$ and $-$ the values at the right and left edge of a cell i, a one-dimensional in space and time Taylor expansion about a cell-center value together with a decomposition in characteristic variables yields:

$$\mathbf{Q_{p_i}}^{+} = \mathbf{Q_{p_i}} + \frac{1}{2}\mathbf{R_i}\left(\mathbf{I_d} - \frac{\Delta t}{\Delta x}\max(\Lambda_i, 0)\right)\Delta\mathbf{z_i}$$

and

$$\mathbf{Q_{p_i}}^{-} = \mathbf{Q_{p_i}} - \frac{1}{2}\mathbf{R_i}\left(\mathbf{I_d} + \frac{\Delta t}{\Delta x}\min(\Lambda_i, 0)\right)\Delta\mathbf{z_i}$$

where $\mathbf{R_i}$ is the matrix of the right eigenvectors associated to the matrix Jacobian $\mathbf{Q_{p_i}}$, Λ_i is the diagonal matrix of the eigenvalues of $\mathbf{Q_{p_i}}$, $\mathbf{I_d}$ the identity matrix, and $\Delta\mathbf{z_i}$ is the *minmod* slope in characteristic variables:

$$\Delta\mathbf{z_i} = \text{minmod}\left(\mathbf{R_i}^{-1}(\mathbf{Q_{p_{i+1}}} - \mathbf{Q_{p_i}}), \mathbf{R_i}^{-1}(\mathbf{Q_{p_i}} - \mathbf{Q_{p_{i-1}}})\right)$$

We propose an extension of 2D Riemann problems from [63], also presented in [64] to the compressible Baer-Nunziato model. The computational domain is $\Omega = [0.5, 0.5] \times [0.5, 0.5]$ and the initial condition is given by four piece-wise constant states defined in each quadrant of the two-dimensional coordinate system in Tab. 4.

These two test-cases are computed using a seventh-order polynomial Discontinuous Galerkin on 100 elements and compared to a second-order TVD-MUSCL Finite Volume on 1600 elements, such that the number of degrees of freedom is the same (6400). The upwind flux function used in either case is the Rusanov flux. A reference

Configuration C_1 ($\gamma_g = 1.4, \pi_g = 0, \gamma_l = 1.4, \pi_l = 0$)									
	α_l	ρ_l	u_l	v_l	p_l	ρ_g	u_g	v_g	p_g
$(x > 0, y > 0)$	0.8	2.0	0.0	0.0	2.0	1.5	0.0	0.0	2.0
$(x < 0, y > 0)$	0.4	1.0	0.0	0.0	1.0	0.5	0.0	1.0	2.0
$(x < 0, y < 0)$	0.8	2.0	0.0	0.0	2.0	1.5	0.0	0.0	2.0
$(x > 0, y < 0)$	0.4	1.0	0.0	0.0	1.0	0.5	0.0	1.0	2.0
Configuration C_2 ($\gamma_g = 1.4, \pi_g = 0, \gamma_l = 3.0, \pi_l = 100$)									
	α_l	ρ_l	u_l	v_l	p_l	ρ_g	u_g	v_g	p_g
$(x > 0, y > 0)$	0.3	1000.0	0.0	0.0	600.0	1.0	0.0	0.0	1.0
$(x < 0, y > 0)$	0.4	800.0	0.0	0.0	500.0	1.5	0.0	1.0	2.0
$(x < 0, y < 0)$	0.3	1000.0	0.0	0.0	600.0	1.0	0.0	0.0	1.0
$(x > 0, y < 0)$	0.4	800.0	0.0	0.0	500.0	1.5	0.0	1.0	2.0

Table 4: Initial conditions for the two-dimensional Riemann problems.

solution is computed using the full non-linear Riemann solver with a zeroth-order polynomial on a grid of one million elements.

Results are displayed in Fig. 10-11 for configuration 1 and 2 respectively. We observe a much better resolution using our artificial viscosity Discontinuous Galerkin discretisation than classical TVD-MUSCL second order Finite Volume with a constant number of degrees of freedom. These test cases are also reported in [64] and compare well qualitatively.

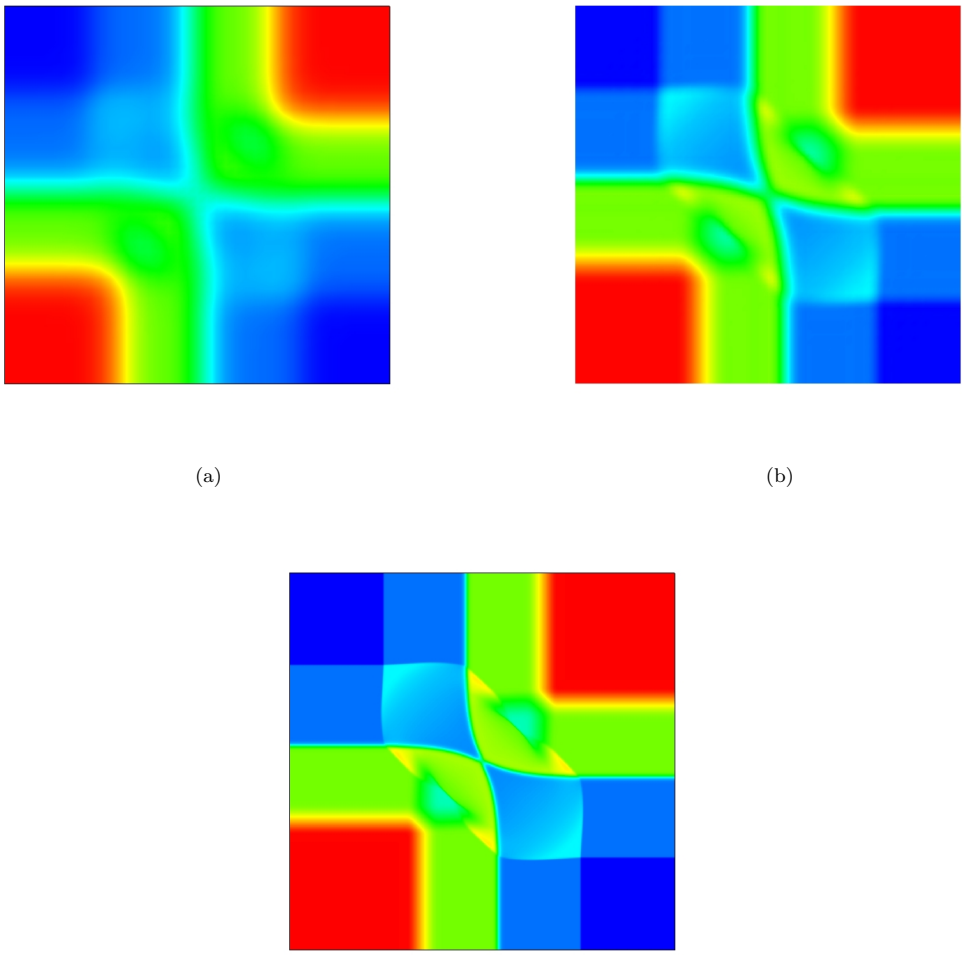

(a) (b)

(c)

Figure 10: C1 test case. Gas density. (a): TVD-MUSCL Finite Volume (1600 elements, N=1), (b): Artificial viscosity Discontinuous Galerkin (100 elements, N=7) and (c): reference solution.

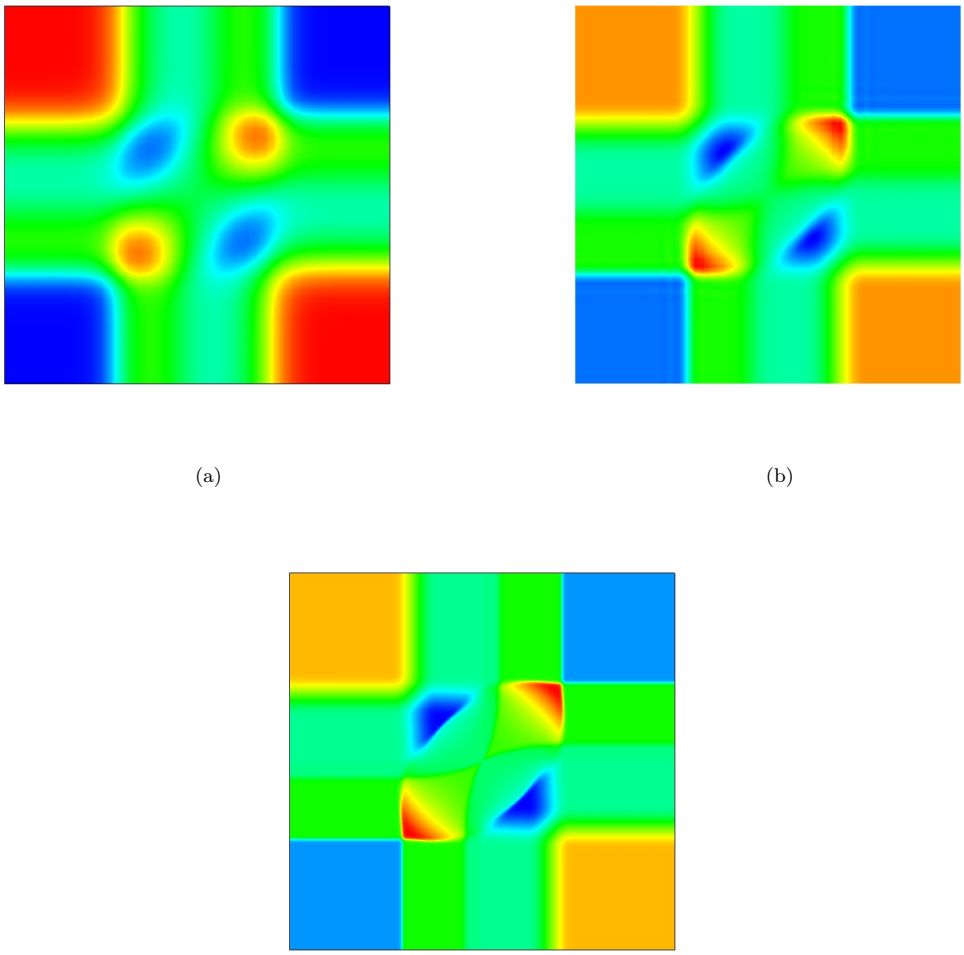

(a) (b)

(c)

Figure 11: C2 test case. Gas density. (a): TVD-MUSCL Finite Volume (1600 elements, N=1), (b): Artificial viscosity Discontinuous Galerkin (100 elements, N=7) and (c): reference solution.

5. Conclusions

Most numerical fluxes developed for the mono-phasic Euler equations may be extended to the two-phase Baer-Nunziato equations thanks to its hyperbolic nature. However, due to the presence of non-conservative products some care should be taken in the discretisation especially in the presence of discontinuities. In this work, we tested several numerical fluxes developed for the Euler equations, based or not on an approximate solution to the Riemann problem associated to the Baer-Nunziato equations, and several techniques were presented to treat the non-conservative products. When the spatial discretisation was first order, strong differences were found between all numerical fluxes. If the Rusanov and GForce fluxes proved to be very robust and computationally cheap, they also generated the most important amount of dissipation of all schemes especially at contact discontinuities. The VFRoe scheme gave very satisfactory results, however there is no clear way of enforcing entropy condition at sonic points: a local Rusanov flux has been used to avoid strong entropy glitches in rarefaction waves. Finally the non-linear Riemann solvers behaved very well on all test cases but their computational cost may become prohibitive when extended to three-dimensions.

Different strategies have been proposed to deal with the presence of non-conservative products. The condition of Abgrall gives a natural numerical scheme to these terms. We extended the Rusanov and GForce flux following this criterion to high-order. The path-conservative formalism allows a clean definition of non-conservative products in the presence of a discontinuity, however we experienced some numerical difficulties on some very demanding test cases, such as positivity preserving issues in strong rarefaction waves. The most robust approach proved to be the Rusanov and GForce fluxes extended to the non-conservative Baer and Nunziato system following the criterion of Abgrall.

In order to deal with the inherent oscillations caused by high-order discretisations in the vicinity of discontinuities, a stabilisation technique based on local artificial viscosity has been adapted to the Baer-Nunziato equations. This approach allowed to smooth the discontinuities in a very thin region and thus resolve them in the space of polynomials. It allowed to compute very high-order solutions to several shock-tube problems. A comparison at equal number of degrees of freedom between our high-order Discontinuous Galerkin approach and a classical TVD-MUSCL Finite Volume reconstruction proved the superiority of the method. Also, it was shown that in the context of high-order reconstruction, the situation changes in a very positive way for the dissipative Rusanov flux which proved to be as accurate as the VFRoe scheme. This result is of great interest, because due to the limited amount of information about the eigenstructure of the flux Jacobian, the Rusanov flux is easy to implement, fast and easily extendable to more complex equations of state.

Future investigations may concern strong shock situations as it is well known that the non-conservative character of the equations usually yield to erroneous shocked states [61, 65]. Further extensions to this work could deal with the development of a Discontinuous Galerkin discretisation to the recent two-phase HLLC solver of Furfaro and Saurel [66].

Acknowledgements

This work has been partially supported by REPSOL under the research grant P130120150 monitored by Dr. Angel Rivero.

AppendixA. Eigenstructure of the Baer-Nunziato model

The Baer-Nunziato model may be written in quasi-linear form:

$$\frac{\partial \mathbf{U}}{\partial t} + \mathbf{A_c}(\mathbf{U})\frac{\partial \mathbf{U}}{\partial x} = 0$$

where $\mathbf{U}$ represents the vector of conservative variables and $\mathbf{A_c}(\mathbf{U})$ takes the form:

$$\mathbf{A_c}(\mathbf{U}) = \begin{bmatrix} u_l & 0 & 0 & 0 & 0 & 0 & 0 \\ 0 & 0 & 1 & 0 & 0 & 0 & 0 \\ -p_g - \gamma_l \pi_l & \hat{\gamma_l} H_l - u_l^2 - a_l^2 & (3-\gamma_l)u_l & -\hat{\gamma_l} & 0 & 0 & 0 \\ u_l(-p_g - \gamma_l \pi_l) & u_l\left(-H_l + \frac{\hat{\gamma_l} u_l^2}{2}\right) & H_l - \hat{\gamma_l} u_l^2 & \gamma_l u_l & 0 & 0 & 0 \\ 0 & 0 & 0 & 0 & 0 & 1 & 0 \\ p_g & 0 & 0 & 0 & \hat{\gamma_g} H_g - u_g^2 - a_g^2 & (3-\gamma_g)u_g & -\hat{\gamma_g} \\ u_l p_g & 0 & 0 & 0 & u_g\left(-H_g + \frac{\hat{\gamma_g} u_g^2}{2}\right) & H_g - \hat{\gamma_g} u_g^2 & \gamma_g u_g \end{bmatrix}$$

with $\hat{\gamma_m} = \gamma_m - 1$, for $m = g, l$. The matrix $\mathbf{A_c}$ has 7 real eigenvalues:

$$\begin{aligned} \lambda_1 &= u_g - a_g \\ \lambda_2 &= u_g, \lambda_3 = u_g + a_g, \lambda_4 = u_l - a_l \\ \lambda_5 &= u_l, \lambda_6 = u_l + a_l, \lambda_7 = u_l \end{aligned} \tag{A.1}$$

and a corresponding set of linearly independent eigenvectors:

$$\mathbf{K_c^1} = \begin{bmatrix} 0 \\ 0 \\ 0 \\ 0 \\ 1 \\ u_g - a_g \\ H_g - u_g a_g \end{bmatrix}, \mathbf{K_c^2} = \begin{bmatrix} 0 \\ 0 \\ 0 \\ 0 \\ 1 \\ u_g \\ \frac{u_g^2}{2} \end{bmatrix}, \mathbf{K_c^3} = \begin{bmatrix} 0 \\ 0 \\ 0 \\ 0 \\ 1 \\ u_g + a_g \\ H_g + u_g a_g \end{bmatrix}$$

$$\mathbf{K_c^4} = \begin{bmatrix} 0 \\ 1 \\ u_l - a_l \\ H_l - u_l a_l \\ 0 \\ 0 \\ 0 \end{bmatrix}, \mathbf{K_c^5} = \begin{bmatrix} 0 \\ 1 \\ u_l \\ \frac{u_l^2}{2} \\ 0 \\ 0 \\ 0 \end{bmatrix}, \mathbf{K_c^6} = \begin{bmatrix} 0 \\ 1 \\ u_l + a_l \\ H_l + u_l a_l \\ 0 \\ 0 \\ 0 \end{bmatrix}$$

$$\mathbf{K_c^7} = \begin{bmatrix} -(\gamma_l - 1)(a_g^2 - (u_g - u_l)^2)\frac{u_l^2}{2} \\ (p_g + \gamma_l \pi_l)(a_g^2 - (u_g - u_l)^2) \\ u_l(p_g + \gamma_l \pi_l)(a_g^2 - (u_g - u_l)^2) \\ 0 \\ \gamma_g \hat{\gamma_l} p_g \frac{u_l^2}{2} \\ \gamma_g \hat{\gamma_l} p_g \frac{u_l^3}{2} \\ \frac{u_l^2}{2}\frac{\hat{\gamma_l}}{\hat{\gamma_g}} p_g \left[a_g^2 - \frac{\hat{\gamma_g}}{2}\left((\gamma_g - 2)(u_g - u_l)^2 - \gamma_g(u_g^2 - u_l^2) - \gamma_g u_g^2\right)\right] \end{bmatrix}$$

Similarly, with the following choice of primitive variables:

$$\mathbf{V} = (\alpha_l, \rho_l, u_l, p_l, \rho_g, u_g, p_g)^T$$

the system of Baer-Nunziato equations may be written in the following quasi-linear form:

$$\frac{\partial \mathbf{V}}{\partial t} + \mathbf{A_p}(\mathbf{V})\frac{\partial \mathbf{V}}{\partial x} = 0$$

where $\mathbf{A_p}(\mathbf{V})$ takes the form:

$$\mathbf{A_p}(\mathbf{V}) = \begin{bmatrix} u_l & 0 & 0 & 0 & 0 & 0 & 0 \\ 0 & u_l & \rho_l & 0 & 0 & 0 & 0 \\ \frac{p_l - p_g}{\alpha_l \rho_l} & 0 & u_l & \frac{1}{\rho_l} & 0 & 0 & 0 \\ 0 & 0 & \rho_l a_l^2 & u_l & 0 & 0 & 0 \\ -\frac{\rho_g}{\alpha_g}(u_g - u_l) & 0 & 0 & 0 & u_g & \rho_g & 0 \\ 0 & 0 & 0 & 0 & & u_g & \frac{1}{\rho_g} \\ -\frac{\rho_g c_g^2}{\alpha_g}(u_g - u_l) & 0 & 0 & 0 & 0 & \rho_g a_g^2 & u_g \end{bmatrix}$$

The corresponding set of eigenvectors read:

$$\mathbf{K_p^1} = \begin{bmatrix} 0 \\ 0 \\ 0 \\ 0 \\ \rho_g \\ -a_g \\ \rho_g a_g^2 \end{bmatrix}, \mathbf{K_p^2} = \begin{bmatrix} 0 \\ 0 \\ 0 \\ 0 \\ 1 \\ 0 \\ 0 \end{bmatrix}, \mathbf{K_p^3} = \begin{bmatrix} 0 \\ 0 \\ 0 \\ 0 \\ \rho_g \\ a_g \\ \rho_g a_g^2 \end{bmatrix}$$

$$\mathbf{K_p^4} = \begin{bmatrix} 0 \\ \rho_l \\ -a_l \\ \rho_l a_l^2 \\ 0 \\ 0 \\ 0 \end{bmatrix}, \mathbf{K_p^5} = \begin{bmatrix} 0 \\ 1 \\ 0 \\ 0 \\ 0 \\ 0 \\ 0 \end{bmatrix}, \mathbf{K_p^6} = \begin{bmatrix} 0 \\ \rho_l \\ a_l \\ \rho_l a_l^2 \\ 0 \\ 0 \\ 0 \end{bmatrix}$$

$$\mathbf{K_p^7} = \begin{bmatrix} \alpha_l \alpha_g a_l^2 (a_g^2 - (u_g - u_l)^2) \\ -\alpha_g (p_l - p_g)(a_g^2 - (u_g - u_l)^2) \\ 0 \\ -\alpha_g (p_l - p_g) a_l^2 (a_g^2 - (u_g - u_l)^2) \\ -\alpha_l \rho_g a_l^2 (u_g - u_l)^2 \\ \alpha_l a_l^2 a_g^2 (u_g - u_l) \\ -\alpha_l \rho_g a_l^2 a_g^2 (u_g - u_l) \end{bmatrix}$$

References

[1] M. Baer, J. Nunziato, A two-phase mixture theory for the deflagration to detonation transition (ddt) in reactive granular materials, International Journal of Multiphase Flow 12.

[2] R. Saurel, R. Abgrall, A multiphase godunov method for compressible multifluid and multiphase flows, Journal of Computational Physics 150 (2) (1999) 425–467.

[3] C. Parès, Numerical methods for nonconservative hyperbolic systems: a theoretical framework, SIAM Journal on Numerical Analysis 44 (2006) 300–321.

[4] D. Schwendeman, C. Wahle, A. Kapila, The riemann problem and a high-resolution godunov method for a model of compressible two-phase flow, Journal of Computational Physics 212 (2) (2006) 490–526.

[5] S. Tokareva, E. Toro, Hllc-type riemann solver for the baer–nunziato equations of compressible two-phase flow, Journal of Computational Physics 229 (10) (2010) 3573 – 3604.

[6] K. Black, A conservative spectral element method for the approximation of compressible fluid flow, Kybernetika 35 (1) (1999) 133–146.

[7] J. S. Hesthaven, High-order accurate methods for time-domain electromagnetics, Advances in imaging and electron physics 127 (2003) 59–125.

[8] T. Lu, P. Zhang, W. Cai, Discontinuous Galerkin methods for dispersive and lossy Maxwell's equations and PML boundary conditions, Journal of Computational Physics 200 (2) (2004) 549–580.

[9] D. A. Kopriva, Metric Identities and the Discontinuous Spectral Element Method on Curvilinear Meshes, Journal of Scientific Computing 26 (3) (2006) 301–327.

[10] D. A. Kopriva, Implementing Spectral Methods for Partial Differential Equations: Algorithms for Scientists and Engineers, springer, 2009.

[11] P.-O. Persson, J. Peraire, Sub-cell shock capturing for discontinuous galerkin methods, Proc. of the 44th AIAA Aerospace Sciences Meeting and Exhibit AIAA-2006-112.

[12] W. H. Reed, T. R. Hill, Triangular mesh methods for the neutron transport equation, Los Alamos Report LA-UR-73-479.

[13] B. Cockburn, G. E. Karniadakis, C.-W. Shu, The development of discontinuous Galerkin methods, Springer, Berlin, Heidelberg, 2000.

[14] B. Cockburn, C.-W. Shu, The Runge–Kutta discontinuous Galerkin method for conservation laws V: multidimensional systems, Journal of Computational Physics 141 (2) (1998) 199–224.

[15] J. Qiu, B. C. Koho, C.-W. Shu, A numerical study for the performance of the rungekutta discontinuous galerkin method based on different numerical fluxes, Journal of Computational Physics 212 (2) (2006) 540–565.

[16] C. Canuto, M. Y. Hussaini, A. Quarteroni, T. A. Zang, Spectral Methods, Fundamentals in Single Domains, Springer, 2006.

[17] R. Eymard, T. Gallouët, R. Herbin, Finite volume methods, Handbook of numerical analysis, 2000.

[18] E. F. Toro, Riemann Solvers and Numerical Methods for Fluid Dynamics, A Practical Introduction, Springer, 2009.

[19] K. Black, Spectral element approximation of convection–diffusion type problems, Applied Numerical Mathematics 33 (1-4) (2000) 373–379.

[20] P. Rasetarinera, M. Y. Hussaini, An Efficient Implicit Discontinuous Spectral Galerkin Method, Journal of Computational Physics 172 (2) (2001) 718–738.

[21] C. Acosta, D. A. Kopriva, Discontinuous Galerkin spectral element approximations on moving meshes, Journal of Computational Physics 230 (5) (2011) 1876–1902.

[22] D. A. Kopriva, S. L. Woodruff, M. Y. Hussaini, Computation of electromagnetic scattering with a non-conforming discontinuous spectral element method, International Journal for Numerical Methods in Engineering 53 (1) (2002) 105–122.

[23] S. Deng, Numerical simulation of optical coupling and light propagation in coupled optical resonators with size disorder, Applied Numerical Mathematics 57 (5-7) (2007) 475–485.

[24] S. Deng, W. Cai, V. Astratov, Numerical study of light propagation via whispering gallery modes in microcylinder coupled resonator optical waveguides, Optics express 12 (26) (2004) 6468–6480.

[25] S. Mao, C. A. Luongo, D. A. Kopriva, Discontinuous Galerkin spectral element simulation of quench propagation in superconducting magnets, Applied Superconductivity, IEEE Transactions on 15 (2) (2005) 1675–1678.

[26] P. Rasetarinera, D. A. Kopriva, M. Y. Hussaini, Discontinuous Spectral Element Solution of Acoustic Radiation from Thin Airfoils, AIAA Journal 39 (11) (2001) 2070–2075.

[27] D. Stanescu, M. Hussaini, F. Farassat, Aircraft engine noise scattering - A discontinuous spectral element approach, in: 40th AIAA Aerospace Sciences Meeting & Exhibit, American Institute of Aeronautics and Astronautics, Reston, Virigina, 2012.

[28] D. Stanescu, J. Xu, M. Y. Hussaini, F. Farassat, Computation of engine noise propagation and scattering off an aircraft, International Journal of Aeroacoustics 1 (4) (2009) 403–420.

[29] N. Castel, G. Cohen, M. Durufle, Application of discontinuous Galerkin spectral method on hexahedral elements for aeroacoustic, Journal of Computational Acoustics 17 (02) (2009) 175.

[30] F. X. Giraldo, J. S. Hesthaven, T. Warburton, Nodal High-Order Discontinuous Galerkin Methods for the Spherical Shallow Water Equations, Journal of Computational Physics 181 (2) (2002) 499–525.

[31] F. X. Giraldo, M. Restelli, A study of spectral element and discontinuous Galerkin methods for the Navier–Stokes equations in nonhydrostatic mesoscale atmospheric modeling: Equation sets and test cases, Journal of Computational Physics 227 (8) (2008) 3849–3877.

[32] M. Restelli, F. X. Giraldo, A conservative discontinuous Galerkin semi-implicit formulation for the Navier-Stokes equations in nonhydrostatic mesoscale modeling, SIAM Journal on Scientific Computing 31 (3) (2009) 2231–2257.

[33] S. Fagherazzi, D. J. Furbish, P. Rasetarinera, M. Y. Hussaini, Application of the discontinuous spectral Galerkin method to groundwater flow, Advances in Water Resources 27 (2) (2004) 129–140.

[34] S. Fagherazzi, P. Rasetarinera, M. Y. Hussaini, Numerical solution of the dam-break problem with a discontinuous Galerkin method, Journal of Hydraulic Engineering 130 (6) (2004) 532–539.

[35] P. D. Lax, Weak solutions of nonlinear hyperbolic equations and their numerical computation, Communications on Pure and Applied Mathematics 7(1) (1954) 159–193.

[36] V. V. Rusanov, The calculation of the interaction of non-stationary shock waves and obstacles, USSR Computational Mathematics and Mathematical Physics 1(2) (1961) 304–320.

[37] E. F. Toro, V. A. Titarev, Musta fluxes for systems of conservation laws, Journal of Computational Physics 216 (2) (2006) 403–429.

[38] E. F. Toro, Riemann solvers with evolved initial conditions, International Journal for Numerical Methods in Fluids 52 (2006) 433–453.

[39] M.-S. Liou, A sequel to ausm: Ausm+, Journal of Computational Physics 129(2) (1996) 364–382.

[40] M.-S. Liou, A sequel to ausm, part ii: Ausm+-up for all speeds, Journal of Computational Physics 214(1) (2006) 137–170.

[41] H. Paillere, C. Corre, J. R. Garcia Cascales, On the extension of the ausm+ scheme to compressible two-fluid models, Computers and Fluids 32 (6) (2003) 891 – 916.

[42] S. Evje, K. Fjelde, On a rough ausm scheme for a one-dimensional two-phase model, Computers & Fluids 32(10) (2003) 1497–1530.

[43] T. Gallouët, T. Masella, A rough godunov scheme, Comptes rendus de l'Académie des Sciences de Paris 323 (1996) 77–83.

[44] T. Gallouët, J. Hérard, N. Seguin, Some recent finite volume schemes to compute euler equations using real gas eos, International Journal for Numerical Methods in Fluids 39 (2002) 1073–1138.

[45] N. Andrianov, Analytical and numerical investigation of two-phase ows, Ph.D. thesis, Fakultät für Mathematik der Otto-von-Guericke Universität Magdeburg (2003).

[46] S. Osher, F. Solomon, Upwind difference schemes for hyperbolic systems of conservation laws, Mathematics of Computation 38 (1982) 339–374.

[47] M. Dumbser, E. F. Toro, A simple extension of the osher riemann solver to non-conservative hyperbolic systems, Journal of Scientific Computing 48(1-3) (2011) 70–88.

[48] B. W. Asay, S. F. Son, J. B. Bdzil, The role of gas permeation in convective burning, International Journal of Multiphase Flow 23(5) (1996) 923952.

[49] E. F. Toro, M. Spruce, W. Speares, Restoration of the contact surface in the hll-riemann solver, Tech. rep., Technical Report CoA-9204. Department of Aerospace Science, College of Aeronautics, Cranfield Institute of Technology (1992).

[50] R. Abgrall, How to prevent pressure oscillations in multicomponent flow calculations: A quasi conservative approach, Journal of Computational Physics 125 (1996) 150–160.

[51] G. Dal Maso, P. G. Lefloch, F. Murat, Definition and weak stability of nonconservative products, Journal de mathématiques pures et appliquées 74 (6) (1995) 483–548.

[52] J. S. Hesthaven, T. Warburton, Nodal discontinuous galerkin methods: algorithms, analysis, and applications, Springer Science and Business Media.

[53] F. Bassi, S. Rebay, A high-order accurate discontinuous finite element method for the numerical solution of the compressible Navier–Stokes equations, Journal of computational physics 131 (2) (1997) 267–279.

[54] B. Cockburn, C.-W. Shu, The local discontinuous galerkin method for time-dependent convection-diffusion systems, SIAM Journal on Numerical Analysis 6 (35) (2006) 2440–2463.

[55] J. Peraire, P.-O. Persson, The compact discontinuous galerkin (cdg) method for elliptic problems, SIAM Journal on Scientific Computing 4 (30) (2008) 1806–1824.

[56] J. Douglas, T. Dupont, Interior Penalty Procedures for Elliptic and Parabolic Galerkin Methods, in: Computing methods in applied sciences, Springer Berlin Heidelberg, Berlin, Heidelberg, 1976, pp. 207–216.

[57] D. N. Arnold, F. Brezzi, B. Cockburn, L. D. Marini, Unified analysis of discontinuous Galerkin methods for elliptic problems, SIAM Journal on Numerical Analysis 39 (5) (2001) 1749–1779.

[58] K. Shahbazi, An explicit expression for the penalty parameter of the interior penalty method, Journal of computational physics 205 (2) (2005) 401–407.

[59] K. Shahbazi, P. F. Fischer, C. R. Ethier, A high-order discontinuous Galerkin method for the unsteady incompressible Navier–Stokes equations, Journal of computational physics 222 (1) (2007) 391–407.

[60] G. A. Sod, A survey of several finite difference methods for systems of nonlinear hyperbolic conservation laws, Journal of Computational Physics 27 (1) (1978) 131.

[61] R. Abgrall, S. Karni, A comment on the computation of non-conservative products, Journal of Computational Physics 229 (8) (2010) 2759–2763.

[62] C. J. Roy, Review of code and solution verification procedures for computational simulation, Journal of Computational Physics 205 (2005) 131–156.

[63] A. Kurganov, E. Tadmor, Solution of two-dimensional riemann problems for gas dynamics without riemann problem solvers, Numerical Methods for Partial Differential Equations 18(5) (2002) 584–608.

[64] M. Dumbser, W. Boscheri, High-order unstructured lagrangian one-step weno finite volume schemes for non-conservative hyperbolic systems: Applications to compressible multi-phase flows, Computers and Fluids 86 (2013) 405 – 432.

[65] R. Abgrall, H. Kumar, Numerical approximation of a compressible multiphase system, Communications in Computational Physics 15 (2014) 1237–1265.

[66] D. Furfaro, R. Saurel, A simple hllc-type riemann solver for compressible non-equilibrium two-phase flows, Computers & Fluids 111 (2015) 159178.